A Dual-Geochronologic and Thermochronologic Detrital Approach to Identify the Focus of Erosion in the Kosi Basin, Nepal

J.N. Zehner[1*], D.A. Orme[1], K. Sundell[2], Y. Najman[3], M. Blum[4], J. Gleason[5], A.K. Laskowski[1], S. Poudel[6]

[1] Department of Earth Sciences, Montana State University, Bozeman, MT

[2] Department of Geosciences, Idaho State University, Pocatello, ID

[3] Lancaster Environment Centre, University of Lancaster, Lancaster, United Kingdom

[4] Department of Geology, The University of Kansas, Lawrence, KS

[5] Department of Earth and Environmental Sciences, University of Michigan, Ann Arbor, MI

[6] Department of Geology, Tri-Chandra Multiple Campus, Tribhuvan University, Kathmandu, Nepal

** Current address: Montana State University, P.O. Box 173480, Bozeman, MT 59717-3480*

Key Points:

- Zircon U-Pb age distributions from the Kosi River are primarily sourced from the lower Lesser Himalayan and Greater Himalayan Sequences.
- Detrital (U-Th)/He thermochronology ages skew younger than the median bedrock age, suggesting high input from mid-latitude/ -altitude regions.
- Combining dating methods suggests a dominant erosive signal consistent with structural models arguing for duplexing over a ramp at depth.

Abstract

The Kosi River watershed captures the major lithotectonic units, structures, and characteristic climatic conditions found along the Himalaya. Therefore, this setting provides a useful location to investigate the respective influences of tectonics and climate in eroding bedrock and driving landscape evolution. Using detrital zircon U-Pb geochronology and low-temperature (U-Th)/He thermochronology, we analyzed modern river sands from the Kosi River and its major tributaries to identify the spatial focus of erosion. Zircon U-Pb geochronological ages from river samples reflect input from all lithotectonic sequences. Six of eight detrital distributions have a dominant age range that is characteristic of the Lesser Himalayan Sequence bedrock age distribution (1700 – 2000 Ma). The furthest downstream sample, thereby the most integrated, has prominent age ranges from 20 – 50 Ma (5%), 400 – 430 Ma (3%), 540 – 570 Ma (4%), 1070 – 1120 Ma (11%), 1790 – 1830 Ma (5%), and 2450 – 2480 Ma (2%). (U-Th)/He low-temperature cooling ages (n = 100) range from 1.2 ± 0.1 to 15.9 ± 0.4 Ma, apart from one grain (55.2 ± 0.7 Ma). The median detrital cooling age is 4.4 Ma, compared to a median bedrock cooling age of 7.6 Ma. Detrital zircon (U-Th)/He ages <6 Ma indicate erosion from central latitudes and mid-elevations in the watershed. Our results suggest that peak erosion occurs north of the dominant precipitation band and south of glaciated high peaks. We interpret these data to support a landscape evolution whereby duplexing along a midcrustal ramp at depth plays a critical role in driving rock uplift and erosion.

Plain Language Summary

The Himalaya are a mountain-building setting in which two continental tectonic plates collided, forcing rocks upward, forming a chain of high elevation peaks. This region also hosts the Indian Summer Monsoon, which causes heavy precipitation. Both processes shape the landscape of this mountain setting, and scientists debate the extent to which tectonic or climate processes control erosion and sediment transport. In this study, we use two methods to analyze sediment within the Kosi River, which drains the high Himalayan peaks surrounding Sagarmatha (Mt. Everest). By understanding the chemical properties of these sediments, we match those properties to known characteristics in the bedrock and determine where the sediment originated. This allows us to understand where the spatial focus of erosion is located. We find that erosion is most dominant at latitudes and elevations that fall between the peak precipitation band and the most glacial cover in present day. Thus, we interpret that tectonic processes below the Earth's surface play a key role in shaping the Himalayan landscape.

1. Introduction

Host to the highest topography on Earth, the Himalayan orogen has remained a focus of geologic research for over one hundred years (e.g., Argand, 1924). Much of this research is fueled by debate over the respective roles and interplay of tectonics and climate in shaping the landscape (e.g., Beaumont et al., 1992; Molnar & England, 1990; Whipple, 2009). One approach to evaluate this landscape evolution is to consider the movement of sediment through watersheds within the orogen by processes of erosion, sediment routing, and deposition (e.g., Blum & Pecha, 2014; Gehrels, 2014; Huntington & Hodges, 2006 ; Olen et al., 2015; Colleps et al., 2018). This can be done by characterizing the age and exhumation history of detrital minerals in modern river sediments in the streams that drain the Himalaya. By comparing the geochronologic and thermochronologic ages of minerals present within modern sediments to existing bedrock ages, it is possible to determine from where material is eroding (e.g., Johnston et al., 2020; Gemignani et al., 2018; Ruhl & Hodges, 2005). In turn, constraining the spatial focus of erosion within a watershed allows for interrogation of the respective roles of tectonics and climate by comparison to known structures and precipitation patterns.

This study focuses on the Kosi River basin, which centers around the Sagarmatha (Mt. Everest) massif, and is a tributary to the Ganges-Brahmaputra source-to-sink sediment routing system (Figure 1a). The Kosi basin captures each of the main lithotectonic sequences and fault structures which exist south of the India-Asia suture zone along strike in the Nepalese Himalaya (Figure 1b; Kapp & DeCelles, 2019; Yin & Harrison, 2000). This basin also features a topographic gradient and precipitation patterns that are broadly comparable to much of the orogen along strike (Whipple et al., 2023). Furthermore, sediment provenance work in this basin benefits from extensive literature characterizing the bedrock geochronology and low-temperature thermochronology, which present usable data to compare to modern river age populations (e.g., Gehrels et al., 2011; Van Der Beek & Schildgen, 2022; Whipple et al., 2023). Considering these lithologic, structural, geomorphological, and climatic conditions—as well as the robust bedrock characterization available— we chose to investigate the spatial focus of erosion within the Kosi basin to test the relative roles of tectonics and climate in driving erosion of the frontal Himalaya.

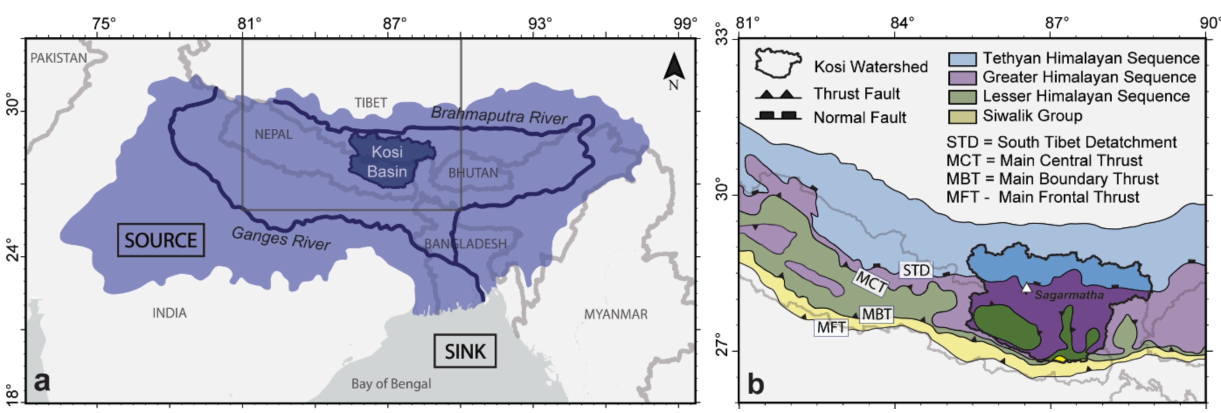

Figure 1. (a) Ganges-Brahmaputra source-to-sink sediment routing system. The area that drains to the Bay of Bengal is blue. The Kosi River watershed is a sub-basin within the larger system, draining eastern Nepal and parts of southern Tibet. Modified from Nicholls et al. (2018). (b) The Kosi basin shown in the context of the regional geology of Nepal. The basin is composed of bedrock from the Tethyan Himalayan Sequence, the Greater Himalayan Sequence, and the Lesser Himalayan Sequence. The watershed contains Sagarmatha (Mt. Everest). Modified from DeCelles et al. (2020).

We present a dual-geochronologic and thermochronologic analysis of sediment generation and routing in Nepal's Kosi watershed to isolate the dominant sediment source region. First, we apply detrital zircon U-Pb geochronology to characterize the age populations present within individual rivers and sub-watersheds within the Kosi Basin. Detrital zircon U-Pb geochronology benefits from large sample sizes (n = 300) and an ability to characterize large and often inaccessible regions challenged by physical and logistical barriers (e.g., Link et al., 2023). Second, we apply zircon (U-Th)/He (ZHe) low-temperature thermochronology to the same samples as a complementary provenance tool, as these ages constrain cooling from mid-crustal and near surface depths (e.g., Ruhl & Hodges, 2005). The application of low-temperature thermochronology has successfully identified the spatial focus of erosion within individual drainages through known age-elevation cooling relationships (e.g., Stock et al., 2006). We leverage the existing bedrock U-Pb and low-temperature thermochronologic data from bedrock studies within the Kosi basin to interrogate the detrital zircon U-Pb and ZHe ages present within individual rivers, sub-watersheds and the entire basin through qualitative and quantitative methods. Through integration of these methods, we interpret the dominant spatial area of erosion within the Kosi basin to reflect the influence of mid-crustal structures within the region.

2. Geologic Setting

2.1 Regional Geology

Nepal's Himalayan geology is broadly characterized as a series of strike-parallel tectonostratigraphic packages south of the India-Asia suture zone, that are bounded by regional scale fault systems. Each fault is representative of a zone of deformation with localized complexities, and different regions include various windows and klippes, creating prominent local heterogeneities. The three geologic packages that make up the bulk of the Nepalese Himalaya are the Tethyan Himalayan Sequence (THS), the Greater Himalayan Sequence (GHS), and the Lesser Himalayan Sequence (LHS) (Yin & Harrison, 2000). The northernmost THS is bounded to the north by the Indus Yarlung suture zone assemblages and Great Counter Thrust system and by the South Tibet Detachment (STD) to the south (Kapp & DeCelles, 2019). The STD is a low-angle normal fault system that was last active as recently as mid-Miocene time (Hodges et al., 1998; Murphy & Harrison, 1999; Orme et al., 2015). This sequence is primarily composed of early Paleozoic to late Precambrian siliciclastic and carbonate sedimentary and metasedimentary rocks (Nakajima et al., 2022; Yin & Harrison, 2000). The GHS is bounded to the north by the STD and to the south by the Main Central Thrust (MCT). The GHS features early Cambrian to late Proterozoic sillimanite grade schists, gneisses, and migmatites, metamorphosed during the Cenozoic Himalayan orogeny, which are generally the highest-grade metamorphic rocks in Nepal, as well as granites of similar age (Nakajima et al., 2022; Olen et al., 2015; Parrish & Hodges, 1996). In addition, there exists a series of leucogranite plutons, dikes, and sills of Miocene-Eocene age (~15-45 Ma) (Cao et al., 2022; Godin et al., 2001; Hodges, 2000; Lavé & Avouac, 2001).

The southernmost tectonic package is the LHS, bounded by the MCT to the north and the Main Boundary Thrust (MBT) to the south. LHS rocks are primarily composed of Precambrian clastic sedimentary and metasedimentary rocks, intruded by ca. 1.8 Ga granitic augen gneisses (Sherpa et al., 2024; Yin & Harrison, 2000). Within the LHS runs the Ramgarh Thrust System. Although thin, this fault system is laterally extensive across all of Nepal, placing older Lesser Himalayan rocks on top of younger Lesser Himalayan and Gondwana Sequence rocks. Terminology describing the LHS varies, generally dependent on if descriptions are based on tectonostratigraphic packages or geographic zones. Most relevant to this study is correlation between rocks described as “Gondwana Sequence” and “upper Lesser Himalayan Sequence.” Some publications use the term Gondwana Sequence to describe Paleocene-Permian age rocks that unconformably overly the lower LHS (e.g. DeCelles et al., 2020; Sherpa et al., 2024). In this report, we use terminology consistent with Gehrels et al. (2011), who describe these rocks as “upper LHS.”

South of the MBT is the Siwalik Group. This group is more than 5,000 m thick and runs along the full extent of the Nepalese Himalaya, representing former foreland basin deposition. The sediments filling this basin were primarily deposited by southward flowing rivers, commonly in the form of large alluvial fans and fluvial systems (DeCelles et al., 1998; Parkash et al., 1980). The Siwalik Group is bounded by the Main Frontal Thrust (MFT) to the south. South of this thrust system in Nepal is dominantly Quaternary sediments.

The concentration of zircons and other heavy minerals is variable amongst these lithotectonic units (Amidon et al., 2005b). However, exact zircon fertility of lithotectonic units is difficult to quantify and further complicated by heterogeneity within respective units. Some efforts seek to quantify bedrock zircon fertility and found it to be generally lowest in the LHS, then THS, and most variable in the GHS, ultimately dividing the latter into two formations due to large variability (Amidon et al., 2005b). Nevertheless, each of these lithotectonic units yields sufficient zircon to characterize the age populations and their unique signatures, regardless of differences in zircon abundance (Gehrels et al. 2011).

Most structural models of the Himalayan orogen propose that these four major surface-breaking faults connect to a single detachment at depth, the Main Himalayan Thrust (MHT). While the MFT, MBT, MCT, and STD are generally well-defined in the literature, there is considerable debate regarding the geometry and location of the Main Himalayan Thrust. The 2015 M_w 7.8 Gorka earthquake in Kathmandu provided valuable data in characterizing this ramp thrust geometry (e.g., Elliott et al., 2016; Hubbard et al., 2016; Lindsey et al., 2018; Whipple et al., 2016). Current models of Main Himalayan Thrust geometry place the ramp structure between 50 – 110 km north of the MFT in the central Himalaya, where this earthquake was located (Elliott et al., 2016; Hubbard et al., 2016; Johnston et al., 2020; Whipple et al., 2016). Many studies have argued that the location of the Main Himalayan Thrust ramp plays a significant role in defining the dominant band of erosion along the orogenic front (e.g., Burbank et al., 2003; Dal Zilio et al., 2019; Elliott et al., 2016; Godard et al., 2014; Grandin et al., 2012; Johnston et al., 2020).

The Kosi region features each of the main lithotectonic units and major fault systems noted above (Figure 2a). Within the watershed, there are three notable tectonic windows in which lower LHS rocks are exposed within the GHS. From west to east, these windows are the Okhaldhunga Window, the Arun Window, and the Taplejung Window (Dhital, 2015). The Okhaldhunga Window is the largest window in Nepal and is occupied by the Great Midland Antiform (Dhital, 2015; Sherpa et al., 2024). Upper LHS rocks make up a small portion of the watershed towards the southern edge of the basin (Figures 2a; 3a). To reiterate, due to variable terminology, these are often mapped as Gondwana Sequence rocks (e.g. Sherpa et al. 2024).

In addition to the main lithotectonic units, the northernmost bedrock makeup of the Kosi watershed, north of the THS, features a small exposure of India-Asia suture zone rocks, including the pre-collisional early Paleogene-Cretaceous subduction complex (Kapp & DeCelles, 2019; Figure 2a). Directly south of this suture zone assemblage and additionally outcropping within the THS are regions of North Himalayan Cretaceous sedimentary rocks. These strata primarily reflect deposition of southerly-derived, supermature quartzose sandstones during the latest Cretaceous (Kapp & DeCelles, 2019). Within both the GHS & THS, there are a series of Miocene-Eocene leucogranites (Cao et al., 2022; Kapp & DeCelles, 2019). Other structures within the watershed include N-S trending extensional faults, most notably associated with the Ama Drime Massif in the northeast region of the Kosi basin (e.g., Jessup et al., 2008; Figure 2a).

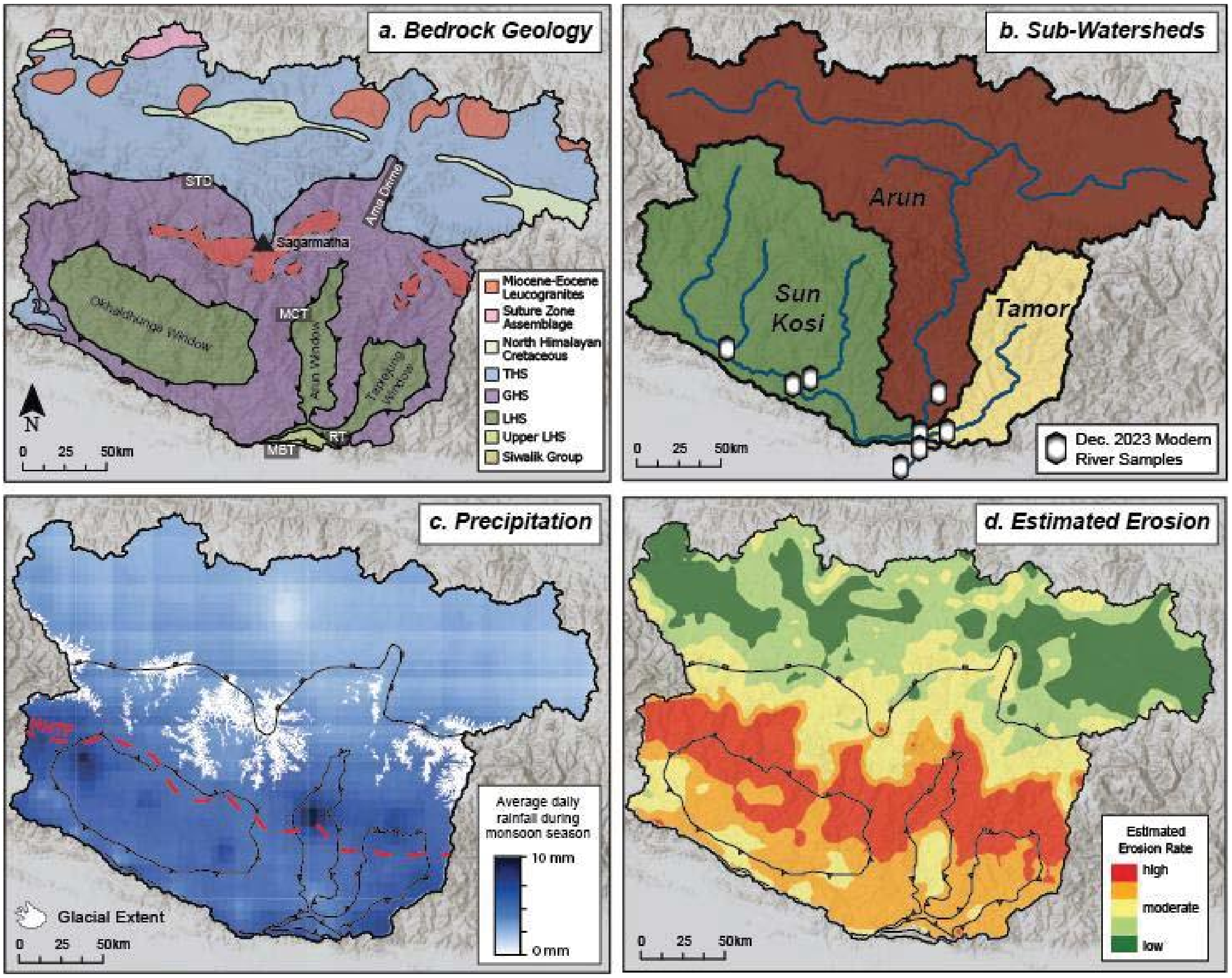

Figure 2. (a) Geologic map of the Kosi basin. Modified from Cao et al. (2022), DeCelles et al. (2020), Hodges (2000), Kapp & DeCelles (2019), Searle & Cottle (2024), and Sherpa et al. (2022). Lithotectonic acronyms included are the Tethyan Himalayan Sequence (THS), Greater Himalayan Sequence (GHS), and Lesser Himalayan Sequence (LHS) (b) Sub-Watersheds for the three main tributaries to the Kosi River: the Sun Kosi, the Arun, and the Tamor (c) Current glacial extent, average rainfall during monsoon season in mm/day, and approximate location of High Himalaya Topographic Front (HHTF). Precipitation data does not include snowfall. Precipitation data from CHIRPS (Climate Hazards group Infrared Precipitation with Stations;

Funk et al., 2015); Glacial extent from GLIMS (Global Land Ice Measurement from Space; GLIMS Consortium, 2005); HHTF location from Whipple et al. (2023) (d) Estimated erosion rate computed from a grid of discharge-based channel steepness, k_{snQ} (Whipple et al., 2023). Categorized from low (green) to high (red) for visual distinction: low (0-25 m/My), moderate-low (25-45 m/My), moderate (45-165 m/My), moderate-high (165-270 m/My), high (>270 m/My).

2.2 Regional Climate and Geomorphology

The modern Himalayan foreland receives heavy, seasonal rainfall from the Indian summer monsoon (e.g., Bookhagen & Burbank, 2010; Gupta & Tandon, 2020; Olen et al., 2015). Although precipitation is greatly concentrated between the months of June throughout September, mean annual rainfall can locally exceed 5 m per year (Olen et al., 2015). The effects of the monsoon are generally heightened in closer proximity to the Bay of Bengal, resulting in high precipitation rates in the Kosi watershed. The northern, high elevation regions of the watershed are arid, receiving minimal precipitation in the form of rainfall (<250 mm/yr; Figure 2c; Bookhagen & Burbank, 2010).

The timing of initiation and intensification of the Indian summer monsoon remains debated. A variety of climate proxies suggest initiation from between 55 Ma to 7.5 Ma, with most interpretations suggesting the monsoon to be established by ~24 Ma (Gupta & Tandon, 2018). Many studies identify an intensification of the monsoon at various points between 15 to 8 Ma (Clift & Webb, 2019; Gupta & Tandon, 2020). Monsoon initiation is interpreted to be driven by both global climatic and tectonic factors, including establishment of modern wind regimes, presence of a permanent Antarctic ice sheet, and the final closure of the Tethyan seaway (Clift &

Webb, 2019; Kennett, 1977; Lawver & Gahagan, 1998). Paleoecology records from Indian Siwalik sediments indicate that the monsoon likely began to weaken ~5 Ma to gradually reach modern conditions (Sanyal et al., 2004). Arguments have also been made for a more recent intensification of the monsoon, from ~2.5–0.9 Ma, as evidenced by increased sedimentation rates (Huntington et al., 2006).

Across strike, there is a sharp topographic transition separating the foothills of the low Himalaya and the rugged high Himalaya, which hosts famous 8,000 m peaks like Sagarmatha and Makalu (Supporting Information). This transition has traditionally been referred to in the literature as “Physiographic Transition 2” (PT2; Hodges et al., 2001), and more recently defined as the “High Himalaya Topographic Front” (HHTF; Whipple et al., 2023; Figure 2c), considering the absence of low Himalaya physiography across the full extent of the orogen. This topographic front is well-documented to be associated with high erosion and exhumation rates (e.g., Burbank et al., 2003; Huntington et al., 2006; Olen et al., 2015). For example, in this zone in the Arun valley, apparent denudation rates reach ~5 mm/yr, accounting for landsliding (Olen et al., 2015). The HHTF area is more variable in both rates and processes when compared to the low and high Himalaya (Olen et al., 2015).

Three main tributaries combine to form the Kosi River, all meeting at one major confluence approximately 15 km northwest of the city of Dharan, Nepal (Figure 2b). From west to east these rivers are the Sun Kosi, the Arun, and the Tamor. Each river is broadly located along a major tectonic window, and all three rivers expose Lesser Himalayan rocks (Dhital, 2015). River profiles vary slightly among the three tributary rivers, reflective of their spatial relationship to the underlying landscape and geologic structures. The Arun River, with a significant portion of the drainage basin reaching to the Tibetan Plateau, hosts two large slope breaks (Figure 2b; Olen et al., 2015). These knickpoints appear to be associated with the location of the STD (Olen et al., 2015; Sonam & Jain, 2018). Neither the Sun Kosi River nor the Tamor River express any obvious knickpoints in river profile (Sonam & Jain, 2018). Han et al. (2024) further attribute the steep nature of the Arun River as a response to a recent (~89 ka) increase in stream power by means of "river piracy," a process that alters water flow and sediment transport routes by reshaping the drainage divide and network. All three tributaries have the highest stream power values when carving through the higher Himalaya. The Arun and Tamor rivers have maximum stream power values between 40,000 to 130,000 W/m, while the Sun Kosi shows a bimodal mode in stream power, reaching a highest total between 25,000 – 40,000 W/m (Sonam & Jain, 2018).

Glacial coverage is widespread at high elevations in the Kosi basin, composing a total area of 3,225 ± 90.3 km^2 according to remote-sensing investigations from 2009 (Shangguan et al., 2014). However, the Kosi basin additionally exhibited one of the fastest rates of glacial retreat in the orogen from 1976-2009 (Shangguan et al., 2014). This retreat is expected to continue, with models estimating between 65-85% decrease in area by 2100 (Khadka et al., 2020). While glacial erosion is known to be a prominent player in contributing to denudation in mountain settings, it remains difficult to quantify (Godard et al., 2012; Olen et al., 2015). In a study of the Marysandi drainage, west of the Kosi watershed, Godard et al. (2012) find significant spatial variation in estimates of glacial erosion rate even within the same catchment, with their upper estimates suggesting an average glacial erosion rate of 5 mm/year in the topographic high Himalaya. All three sub-watersheds in the Kosi basin capture glaciated high peaks where these erosive forces may be at play, with the most glacial coverage found in the Dudh Kosi watershed and the Tethyan portions of the Arun watershed.

2.3 Existing Kosi Watershed Bedrock Ages

This project benefits from a large quantity of previous studies that have analyzed regional bedrock to determine crystallization and lower temperature cooling ages. We compare the published bedrock zircon cooling and crystallization age data to our modern river samples.

2.3.1 U-Pb Geochronology

Bedrock U-Pb geochronological ages for this study are grouped by major lithotectonic unit and compiled by Gehrels et al. (2011). These ages are reported as composite distributions for THS and upper LHS, GHS, and lower LHS, and are compiled from published U-Pb geochronological datasets across the Himalayan orogen. We report dominant age ranges by lithotectonic unit within the following text.

To maintain consistency with distributions reported in Gehrels (2011), we use the terminology "THS and upper LHS," noting that the upper LHS bedrock included in this composite is commonly stratigraphically referred to as the Gondwana Sequence. THS strata are combined with upper LHS strata due to stratigraphic correlation between units and strong similarity from the Cretaceous through the Cambrian age spectra (Gehrels et al. 2011). Dominant age ranges of the THS and upper LHS include 480 – 570 Ma, 750 – 1200 Ma, and 2430 – 2560 Ma (Figure 3b; Gehrels et al., 2011). GHS strata show relative modes at 800 – 1200 Ma, 1600 – 1900 Ma, and 2400 – 2700 Ma. About half of the samples from the GHS included in this compilation also contain 540–750 Ma grains, reflective of Cambro-Ordovician granites present in this unit (Gehrels et al 2011). The lower LHS strata are composed entirely of older grains, reporting dominant ages between 1700 – 2000 Ma and 2400 – 2800 Ma (Gehrels et al., 2011).

As noted, within the THS and GHS are young leucogranite bodies. U-Pb ages of leucogranites in the GHS range from 12 – 23 Ma (Cao et al., 2022; Hodges, 2000). THS leucogranites are generally older, ranging from 33 – 45 Ma, with ages >38 Ma overlapping with the tail-end of Gangdese magmatic arc magmatism, north of the suture zone in southern Tibet (Cao et al., 2022; Kapp & DeCelles, 2019).

2.3.2 Low-Temperature Thermochronology

Numerous studies have applied low-temperature thermochronology to bedrock within the Kosi basin with the goal of quantifying rates of exhumation (e.g., Jessup et al., 2008; Nakajima et al., 2022; Streule et al., 2012; Wang et al., 2010). These studies use a range of thermochronometric systems including apatite fission track, apatite (U-Th)/He, zircon fission track (ZFT), and zircon (U-Th)/He (ZHe), collectively covering a thermal window between ~280-40^{o} C (e.g., Reiners, 2004). Zircon low-temperature data (ZFT and ZHe) are the most abundant and offer the greatest spatial coverage across the basin (Figure 3). In addition, previous applications of ZHe within the Himalayan system document the reproducibility of detrital ZHe dates to successfully capture age populations found within the bedrock ZHe record (e.g., Colleps et al. 2018).

Owing to the documented high rates of exhumation within this region (e.g., 1-4 mm/yr; Huyghe et al. 2020; Long et al., 2012), we elected to combine both ZFT and ZHe ages to increase the size and spatial resolution of our bedrock dataset, despite the resulting broader range in closure temperature (Figure 3a). ZFT has a closure temperature range of ~180 – 350°C and ZHe has closure temperature between ~140 – 200°C (Guenthner et al., 2013; Reiners et al., 2004; Yamada et al., 1995). From south to north, there is an initial general decrease in cooling age towards the center of the watershed, followed by an increase in age northward across the

STD (Figure 3a). Specifically, south of the structural windows, the oldest mean ZFT cooling age is 12.7 Ma (Nakajima et al., 2020). North of the Okhaldhunga window, within the latitudinal middle of the watershed, the youngest ZHe ages are found, yielding ages as young as 1.4 ± 0.05 Ma (ZHe mean age; McDermott et al., 2013). North of the STD, in the Rongbuk Valley north of Sagarmatha, ZHe ages are between ~14-17 Ma (Orme et al. 20215). Ages are broadly latitudinally consistent from west to east in the southern portion of the watershed, but show variation to the north, specifically with younger cooling ages reflecting more recent extension and exhumation in the Ama Drime region (Figure 3a; Jessup et al., 2008; McDermott, 2012). This bedrock data emphasizes the many heterogeneities in cooling age in this structurally complex area. Furthermore, it highlights that many of these complexities may not be shown by the resolution of existing thermochronological data, as we are reliant on where past projects have been focused.

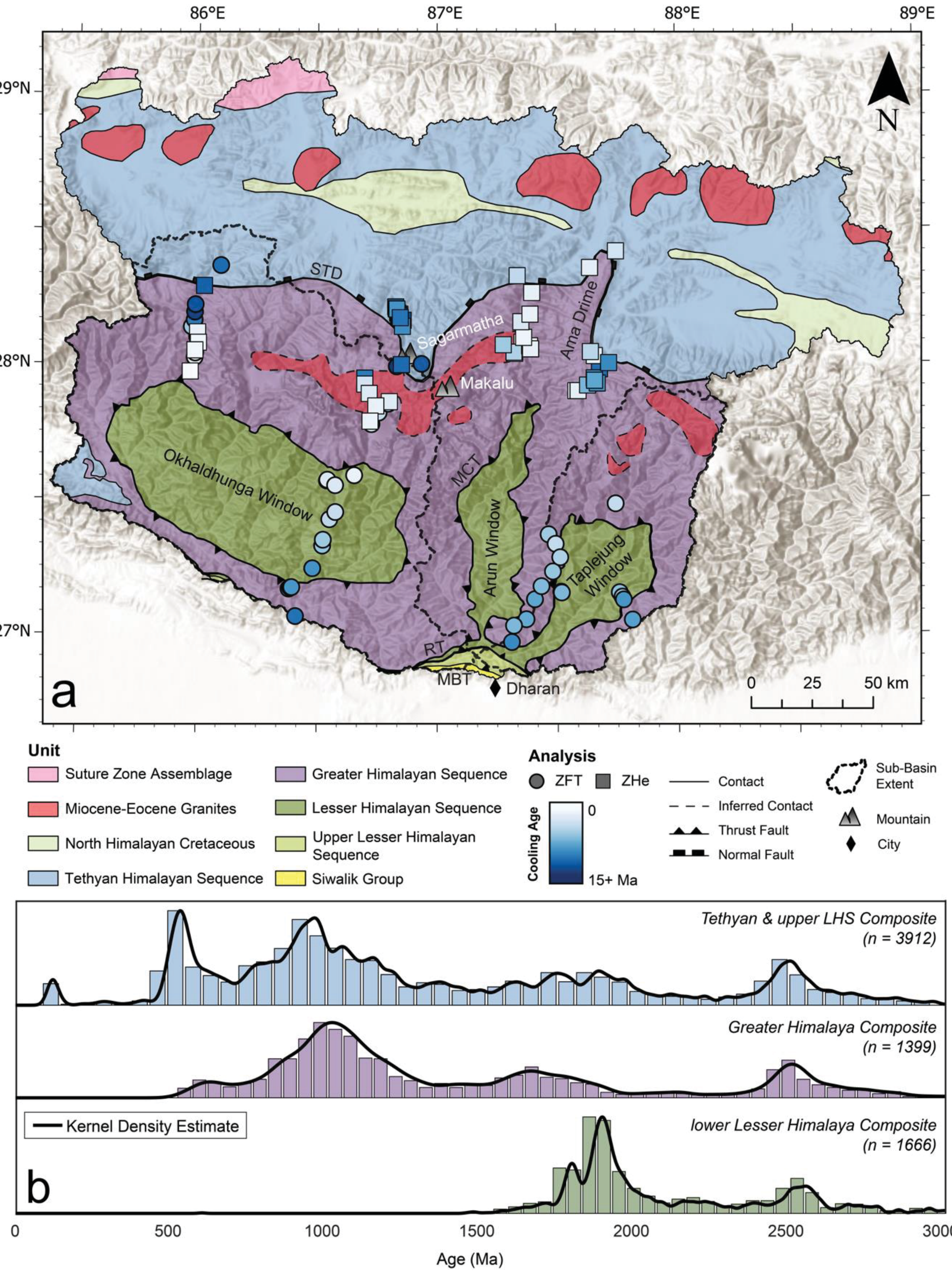

86ºE
87ºE
88ºE
89ºE
29ºN
28ºN
27ºN
N
STD
Sagarmatha
Makalu
Ama Drime
Okhaldhunga Window
MCT
Arun Window
Taplejung Window
RT
MBT
Dharan
0 25 50 km
a
Unit
Suture Zone Assemblage
Miocene-Eocene Granites
North Himalayan Cretaceous
Tethyan Himalayan Sequence
Greater Himalayan Sequence
Lesser Himalayan Sequence
Upper Lesser Himalayan Sequence
Siwalik Group
Analysis
ZFT
ZHe
Cooling Age
0
15+ Ma
Contact
Inferred Contact
Thrust Fault
Normal Fault
Sub-Basin Extent
Mountain
City
Tethyan & upper LHS Composite
(n = 3912)
Greater Himalaya Composite
(n = 1399)
Kernel Density Estimate
lower Lesser Himalaya Composite
(n = 1666)
b
0
500
1000
1500
2000
2500
3000
Age (Ma)

Figure 3. (a) Published zircon (U-Th)/He (ZHe) and zircon fission track (ZFT) low-temperature thermochronological data in the Kosi region, shown in reference to the major tectonic units and rivers. Geologic map modified from Cao et al. (2022), Hodges (2000), Kapp & DeCelles (2019), Searle & Cottle (2024), and Sherpa et al., (2022). Bedrock ages sourced from McDermott (2012), McDermott et al. (2013), Nakajima et al. (2020), Nakajima et al. (2022), Orme et al. (2015), Sakai et al. (2005), Sakai et al. (2013), Schultz (2017), Schultz et al. (2017), Streule et al. (2012), and Wang et al. (2010) (b) Kernel density estimates for zircon U-Pb ages for the Tethyan strata and upper Lesser Himalayan strata, Greater Himalayan strata, and lower Lesser Himalayan strata (Gehrels, 2011).

The oldest bedrock cooling ages to the south are 12.7 Ma (ZFT mean age; Nakajima et al., 2020). The youngest ages are broadly found in the middle of the watershed, by latitude, with a youngest reported age of 1.4 ± 0.05 Ma (ZHe mean age; McDermott et al., 2013). Cooling ages increase again when moving across the STD into the northernmost recorded ages in the watershed. For example, Orme et al. (2015) find ZHe ages between ~14-17 Ma in the Rongbuk Valley north of Sagarmatha. While thermochronological ages show broad consistency along strike (e.g., Whipple et al., 2023), there are also local differences. This bedrock data emphasizes the many heterogeneities in cooling age in this structurally complex area. Furthermore, it highlights that many of these complexities may not be shown by the resolution of existing thermochronological data, as we are reliant on where past projects have been focused.

3.0 Methods

3.1 Overview and Sample Collection

To investigate sediment generation and routing in the Kosi basin, we sampled modern river sands from each of the major tributaries within the watershed. We characterized single detrital zircon grains extracted from bulk sediment samples using U-Pb geochronology and (U-Th)/He low-temperature thermochronology. We compare these cooling and crystallization ages to published bedrock dates and cross-comparison with other sediment samples collected in this study (Gehrels, 2014). The application of low-temperature thermochronology to decipher the provenance of sediment in modern river systems remains less extensive (e.g., Carrapa et al., 2017) and is often applied to small drainage basins with direct cooling age-elevation relationships (e.g., Ruhl & Hodges, 2005; Stock et al., 2006). Therefore, we pair geochronology with low-temperature thermochronology to take advantage of the strengths of each method and provide an integrated dataset to better match detrital grains to their original host rock (e.g., Peyton & Carrapa, 2013).

We collected 10 modern river samples: eight from tributaries that feed the Kosi River and two post-confluence samples from the Kosi River (NP23-01, NP23-06; Figure 4). Four samples were collected from the Sun Kosi system (NP23-05 Sun Kosi, NP 23-08 Dudh Kosi, NP23-09 Sun Kosi, and NP23-10 Tama Kosi). Two samples were collected from the Arun River (NP23-03, NP23-04) and two samples from the Tamor River (NP23-02, NP23-07). Bulk sediment samples were separated by ZirChron LLC to isolate zircon grains using standard mineral separation processes (e.g., Gehrels, 2008). Single zircons were dated separately for low-temperature thermochronology and U-Pb geochronology.

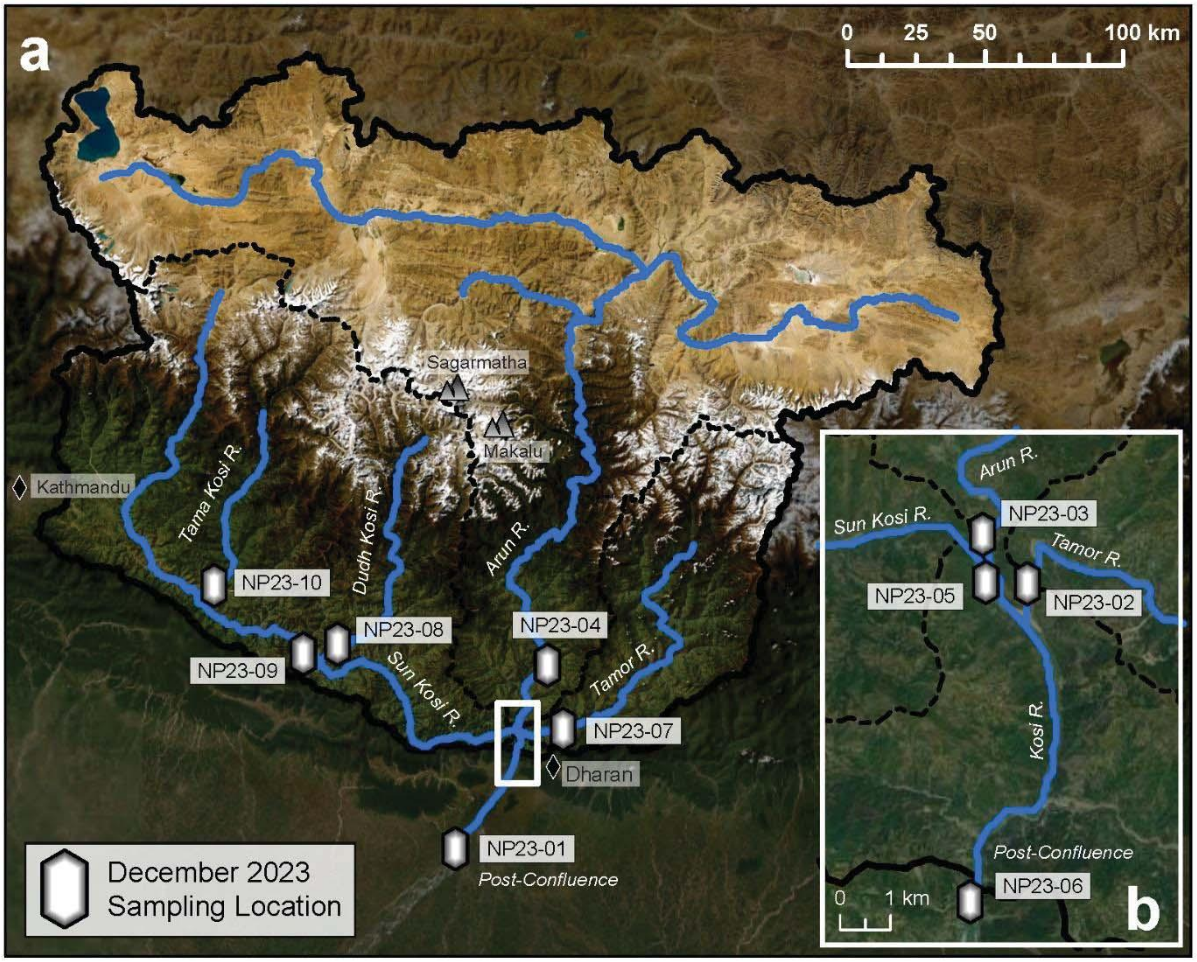

Figure 4. (a) Sampling locations of modern river sands analyzed in this study at the watershed scale. (b) Inset showing sampling locations immediately pre- and post-confluence of major tributaries.

338 *3.2 Detrital Zircon U-Pb Geochronology*

339 Zircon U-Pb geochronology through laser ablation-inductively coupled plasma-mass
340 spectrometry (LA-ICP-MS) is based on three different decay systems: $^{238}U/^{206}Pb$, $^{235}U/^{207}Pb$, and
341 $^{232}Th/^{208}Pb$ (Gehrels, 2014), each of which provides an independent crystallization age of the
342 zircon mineral. In turn, a fourth date is generated through the combination of two decay schemes,

producing a ^{206}Pb/^{207}Pb date. Based on the respective decay constants of each system, ^{238}U/^{206}Pb ages are used for < 1200 Ma ages and ^{206}Pb/^{207}Pb ages are used for > 1200 Ma ages (Gehrels et al., 2008). We analyzed 9 of 10 bulk samples for detrital zircon U-Pb geochronology, excluding NP23-07 due to proximity to sample NP23-02 along the Tamor River. Single-spot U-Pb crystallization ages were obtained at The University of Arizona LaserChron Center, following their standard laboratory procedures (Gehrels et al., 2008). The number of grains analyzed per sample ranged from 147 grains (NP23-04) to 530 grains (NP23-01) with > 300 grains analyzed for 7 of 9 samples to characterize the age distributions and relative abundance of age peaks (Supporting Information).

3.3 Detrital zircon (U-Th)/He thermochronology

Low-temperature thermochronology constrains when rocks cool toward Earth's surface, generally by processes of erosion or tectonically driven exhumation (Reiners et al., 2004; Reiners & Brandon, 2006). This method uses a mineral's closure temperature, defined as the range of temperatures within which the daughter product is retained in a crystal (Dodson, 1973). Zircon (U-Th)/He low-temperature thermochronology uses the same U-Th-Pb decay scheme as U-Pb geochronology, which generates ^{4}He atoms via alpha decay along their decay chain to their final Pb daughter products (Flowers et al., 2023). ZHe has a closure temperature between ~140–200°C (Guenthner et al., 2013; Reiners et al., 2004), making it useful to investigate cooling histories in rapidly exhuming landscapes such as the Himalaya (e.g., Colleps et al., 2018; Long et al., 2012).

To obtain (U-Th)/He low-temperature cooling ages, we followed standard laboratory procedures of grain selection, helium degassing, dissolution, and data reduction (Flowers et al., 2023). Individual grains were selected and packed in Nb packets at the Montana State University Tectonic Sedimentary and Thermochronology laboratory. Picked grains were prioritized to be inclusion-free, euhedral, and clear (Reiners et al. 2002). Helium degassing, crystal dissolution, and data reduction occurred at the University of Colorado TRaIL lab from July-September 2024, following their standard laboratory procedures (Flowers et al., 2023). Double-dating of the same zircon analyzed for U-Pb was not pursued after initial attempts to pluck the zircons from the grain mounts highlighted the variable degree of polishing amongst a wide range of grain sizes (i.e., many grains were polished so that >50% of the grain was removed, which would result in an erroneous alpha-ejection correction using standard dissolution methods (e.g. Rahl et al., 2003; He and Reiners, 2022). We analyzed 10 zircon grains per sample for (U-Th)/He low-temperature thermochronology for all tributary samples. For our post-confluence sample, we analyzed 20 grains from NP23-06, due to low zircon yield for the further downstream post-confluence sample, NP23-01. This resulted in a dataset of 100 ZHe cooling ages.

ZHe ages often show much greater scatter than analytical precision would suggest (e.g., Reiners, 2004; Farley et al., 1996). Known sources of potential age scatter include He implantation from external phases or inclusions (Murray et al. 2014; Spiegel et al. 2009), alpha-ejection correction assumptions (Vermeesch, 2012; Zeigler et al. 2024), and radiation damage (Guenthner et al. 2013; Diver et al. 2021). With our dataset, we investigate potential sources of age scatter before interpreting any geologic significance. In addition, detrital studies across the Himalaya vary greatly in their n values, but studies using as low as n = 22 ZHe ages successfully reproduce known bedrock ZHe age populations (Colleps et al. 2018). Therefore, we do compare our detrital (n = 100) dataset to existing bedrock records for geologic interpretation but discuss potential limitations of statistical analyses.

3.4 Statistical Analysis

We performed multidimensional scaling (MDS) analysis on each of the U-Pb and ZHe crystallization and cooling age distributions to visualize the (dis)similarity among detrital zircon age distributions. This method maps samples as points in Cartesian space by transforming sample dissimilarity into Euclidian distance (Vermeesch, 2013). More alike samples plot closer to each other, with greater distances between points representing greater sample dissimilarity. We used the MATLAB-based program, DZmds, to produce these maps (Saylor et al., 2017). Also included on the MDS maps are arrows to denote the nearest-neighbor distribution to each sample. We use the cross-correlation metric for U-Pb datasets and the Kuiper test for ZHe datasets. The cross-correlation coefficient represents the R^2 value of a crossplot of finite mixture distribution quantiles. The Kuiper test V-statistic is calculated by summing the maximum distance between two CDFs (Sundell & Saylor, 2017).

To further characterize the relationship between samples, we ran a series of Inverse Monte Carlo mixture models. The goal of this analysis is to statistically compare tributary river sands to the post-confluence sample, using the MATLAB-based program, DZmix (Sundell & Saylor, 2017). This model compares one mixed sample (in our case, the post-confluence sample) to multiple potential source samples (tributary river sands) and reports best-fit percent contributions from each source (e.g. Link et al., 2023). We completed four MDS analyses and four mixture models. U-Pb analyses use the composite post-confluence age distribution (combined NP23-01 & NP23-06) to represent the post-confluence sediment profile. ZHe analyses use the twenty grains dated from NP23-06 to represent the post-confluence sediment profile (NP23-06). A breakdown of the model parameterizations is as follows, in which each listed parameterization represents an MDS and mixture analysis:

1. U-Pb: NP23 post-confluence composite compared to NP23 modern river sands, by sample
2. U-Pb: NP23 post-confluence composite compared to NP23 modern river sands, by watershed
3. ZHe: NP23 post-confluence sample compared to NP23 modern river sands, by sample
4. ZHe: NP23 post-confluence sample compared to NP23 modern river sands, by watershed

Noting the small sample sizes incorporated into these models from our thermochronological data, we consider our helium model results with caution. While mixture model results offer additional quantitative insight on potential sediment sourcing, especially when paired with MDS analyses, we are conservative in our interpretations and consider the results in geologic context. MDS analyses and mixture models for U-Pb data and ZHe data using bedrock ages as potential sources are found in Supporting Information. These bedrock-detrital models are a useful exercise, but we caution against using the percentages produced as the bedrock input in a composite of all zircon U-Pb data from across the orogen, not Kosi watershed specific. Therefore, we prioritize a qualitative approach to comparing detrital and bedrock records for the U-Pb data.

4.0 Results

New data include U-Pb geochronological age distributions for 9 of 10 detrital samples and (U-Th)/He thermochronological ages for 9 of 10 detrital samples (Figure 5). We present these profiles by sample, sub-watershed, and for the full Kosi basin. We report MDS analyses and mixture model results for each of the four scenarios described above.

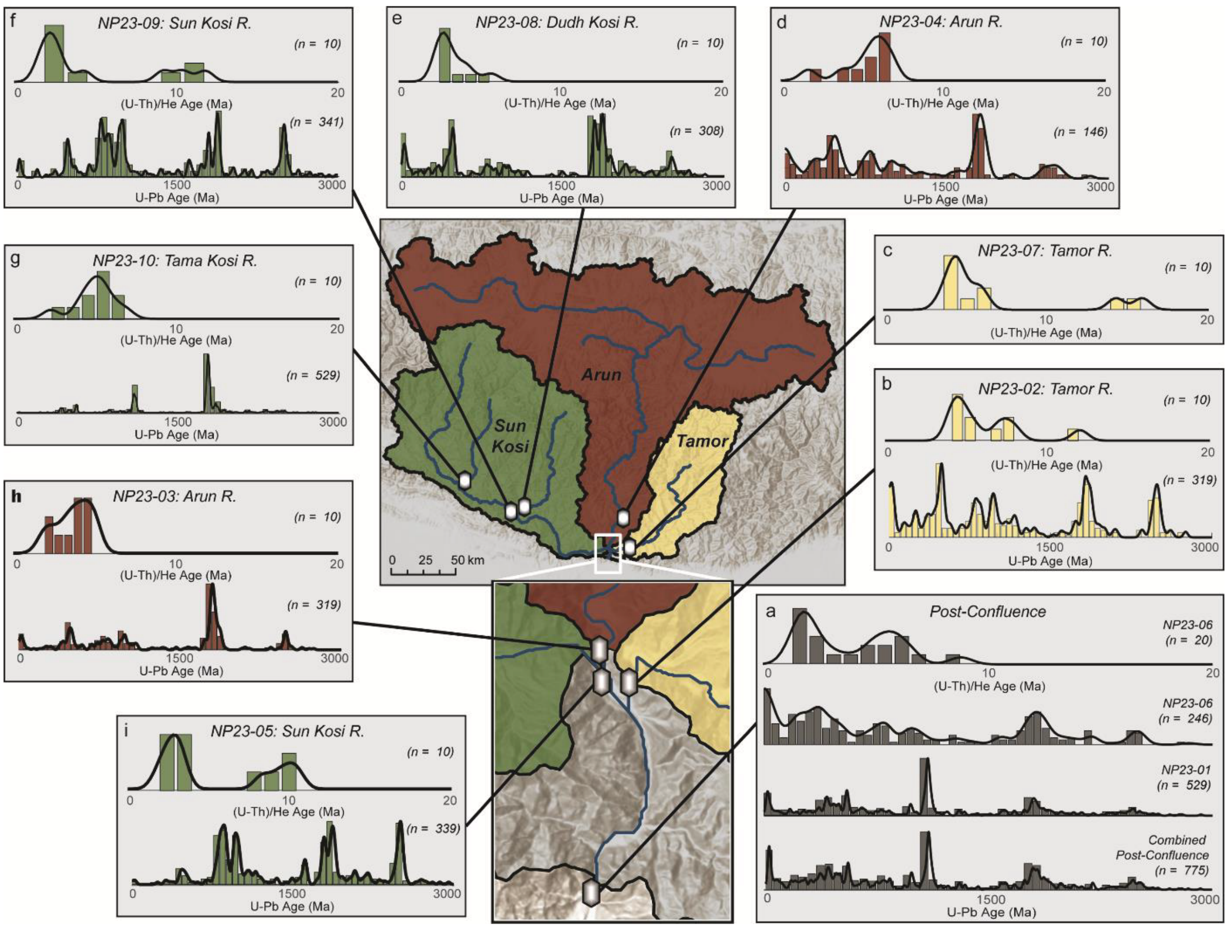

Figure 5. U-Pb Geochronological data and (U-Th)/He Thermochronological data by sample location. (a) Post-confluence (b) NP23-02: Lower Tamor (c) NP23-07: Upper Tamor (d) NP23-04: Upper Arun (e) NP23-08: Dudh Kosi (f) NP23-09: Upper Sun Kosi (g) NP23-10: Tama Kosi (h) NP23-03: Lower Arun (i) NP23-05: Lower Sun Kosi

434

435 *4.1 U-Pb Geochronology of Modern River Sands*

U-Pb age distributions of detrital samples reflect known bedrock ages from all major lithotectonic terranes in the Kosi watershed (Figure 6; Table 1). Element concentrations and calculated ages by individual grain can be found in Supporting Information.

As noted, we elect to combine both of our post-confluence samples into one composite sample of 775 grains, due to their relative similarity. This composite sample has prominent age ranges between 15 – 50 Ma, 400 – 430 Ma, 540 – 570 Ma, 1070 – 1120 Ma, 1790 – 1830 Ma, and 2450 – 2480 Ma (Figure 6). Paleozoic and Proterozoic age ranges correlate to known dates from the major lithotectonic units (Gehrels et al., 2011) and the youngest 15 – 50 Ma age peak broadly correlates with the wide age range of leucogranites in the GHS and THS. The dominant age range of the post-confluence sample is 1070 – 1120 Ma, which aligns with ages from the GHS (800 – 1200 Ma) or THS / upper LHS (750 – 1200 Ma). This age range is also present in the Siwalik Group, the sedimentary unit which composes most of the bedrock between post-confluence sampling locations (Baral et al., 2015).

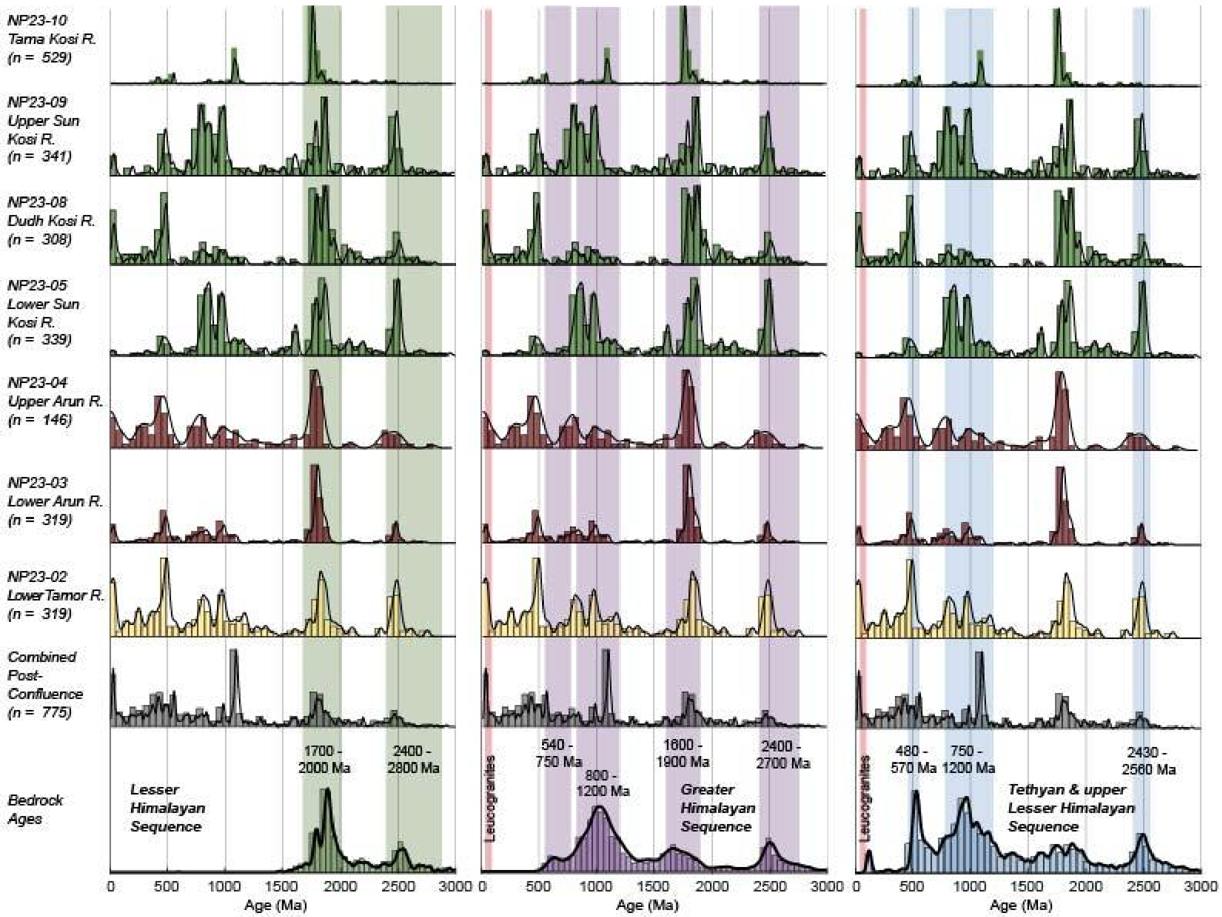

Figure 6. Detrital zircon U-Pb age distributions by sample compared to bedrock ages, with known age peaks by unit highlighted (Gehrels et al., 2011).

Geochronologic ages ranges are largely consistent between all samples, with variation in the relative proportionality of ages (Table 1). The most consistent age range among samples is 1600 – 2000 Ma, which is the dominant age range in six of eight samples and is present in all samples (Figure 6). Each sample contains young grains <50 Ma, forming a relative mode in five of eight samples (Figure 6). The abundance and age range of these young grains varies by sample, with the dominant age range between 15 – 35 Ma, and a scattering of grains between 40 – 50 Ma (Table 1).

Table 1. Prominent U-Pb age ranges present in each detrital sample. Included is their relative abundance (compared to other age ranges within the same distribution) and overlapping age ranges within bedrock age composite distributions (Gehrels et al., 2011). THS: Tethyan Himalayan Sequence; uLHS: upper Lesser Himalayan Sequence; LHS: Lesser Himalayan Sequence; GHS: Greater Himalayan Sequence.

Sample	**Dominant Age Range**	**Relative Ranking in Abundance**	**Overlapping Bedrock Age Ranges**
Post-Confluence Composite	15 – 50 Ma	2	Leucogranite intrusions
	400 – 430 Ma	4	Ages present in THS/uLHS as a non-dominant age range
	540 – 570 Ma	5	480 – 570 (THS/uLHS), 540 – 750 (GHS)
	1070 -1120 Ma	1	750 – 1200 (THS/uLHS), 800 – 1200 (GHS)
	1790 – 1830 Ma	3	1700 – 2000 (LHS), 1600 – 1900 (GHS)
	2450 – 2480 Ma	6	2400 – 2800 (all bedrock units)
Lower Tamor (NP23-02)	16 – 30 Ma	3	Leucogranite intrusions
	470 – 510 Ma	1	480 – 570 (THS/uLHS)
	790 – 820 Ma	6	750 – 1200 (THS/uLHS), 800 – 1200 (GHS)
	950 – 1000 Ma	5	750 – 1200 (THS/uLHS), 800 – 1200 (GHS)
	1820 – 1880 Ma	2	1700 – 2000 (LHS), 1600 – 1900 (GHS)
	2450 – 2520 Ma	4	2400 – 2800 (all bedrock units)
Lower Arun (NP23-03)	15 – 35 Ma	4	Leucogranite intrusions
	470 – 510 Ma	2	480 – 570 (THS/uLHS)
	780 – 830 Ma	6	750 – 1200 (THS/uLHS), 800 – 1200 (GHS)
	960 – 1000 Ma	3	750 – 1200 (THS/uLHS), 800 – 1200 (GHS)
	1760 – 1830 Ma	1	1700 – 2000 (LHS), 1600 – 1900 (GHS)
	2460 – 2510	5	2400 – 2800 (all bedrock units)
Upper Arun (NP23-04)	15 – 35 Ma	3	Leucogranite intrusions
	450 – 500 Ma	2	480 – 570 (THS/uLHS)

	820 – 860 Ma	4	750 – 1200 (THS/uLHS), 800 – 1200 (GHS)
	1760 – 1840	1	1700 – 2000 (LHS), 1600 – 1900 (GHS)
	2460 – 2510 Ma	5	2400 – 2800 (all bedrock units)
Lower Sun Kosi (NP23-05)	17 – 29 Ma	6	Leucogranite intrusions
	450 – 500 Ma	5	480 – 570 (THS/uLHS)
	820 – 880 Ma	3	750 – 1200 (THS/uLHS), 800 – 1200 (GHS)
	1600 – 1630 Ma	4	1600 – 1900 (GHS)
	1800 – 1900 Ma	1	1700 – 2000 (LHS), 1600 – 1900 (GHS)
	2430 – 2530 Ma	2	2400 – 2800 (all bedrock units)
Dudh Kosi (NP23-08)	13 – 50 Ma	3	Leucogranite intrusions
	430 – 500 Ma	2	480 – 570 (THS/uLHS)
	780 – 1000 Ma	5	750 – 1200 (THS/uLHS), 800 – 1200 (GHS)
	1760 – 1860 Ma	1	1700 – 2000 (LHS), 1600 – 1900 (GHS)
	2480 – 2700 Ma	4	2400 – 2800 (all bedrock units)
Upper Sun Kosi (NP23-09)	15 – 35 Ma	6	Leucogranite intrusions
	460 – 500 Ma	5	480 – 570 (THS/uLHS)
	760 – 810 Ma	3	750 – 1200 (THS/uLHS), 800 – 1200 (GHS)
	860 – 1000 Ma	2	750 – 1200 (THS/uLHS), 800 – 1200 (GHS)
	1850 – 1900 Ma	1	1700 – 2000 (LHS), 1600 – 1900 (GHS)
	2460 – 2520 Ma	4	2400 – 2800 (all bedrock units)
Tama Kosi (NP23-10)	480 – 570 Ma	3	480 – 570 (THS/uLHS)
	1070 – 1150 Ma	2	800 – 1200 (GHS)
	1750 – 1880 Ma	1	1700 – 2000 (LHS), 1600 – 1900 (GHS)

In addition to assessing each sample signal individually, we combine sample age distributions by watershed to create composite age comparison by major tributary. With these groupings, both the post-confluence and Tamor signals remain the same because only one sample/composite sample exists from each, and therefore there is no required new composite for either distribution. The Arun composite sample closely resembles both individual Arun sample distributions, with a dominant age range from 1600 – 2000 Ma. Individual Sun Kosi watershed sample distributions are more variable when compared to each other. Most notably, age distributions of the main stem of the Sun Kosi, NP23-05 and NP23-09, have prominent age ranges from ~750 – 1200 Ma, which are absent from the two Sun Kosi tributary samples (Dudh Kosi R. and Tama Kosi R.). The composite age distribution for the Sun Kosi watershed reflects this age range but offers a reminder of the variability in sediment profile throughout the watershed.

4.2 Low-Temperature Thermochronology of Modern River Sands

One-hundred grains analyzed for zircon (U-Th)/He thermochronology range from 1.2 ± 0.1 to 15.9 ± 0.4 Ma, except for one grain from the upper Arun sample that returned an age of 55.2 ± 0.7 Ma. Data show potentially two young, latest Miocene to Pleistocene age ranges, from 1.5 – 3.0 Ma and 4.5 – 7.0 Ma (Figure 7), with 76% of ages being less than 6 Ma. The median age is 4.4 Ma. There is no correlation between age and grain size, effective Uranium (eU, a proxy for radiation damage), or the presence of visible inclusions during grain selection (Supporting Information). However, it is plausible that known controls on single ZHe ages, such as the effects of radiation damage, may not be observed with n = 100 versus a larger dataset.

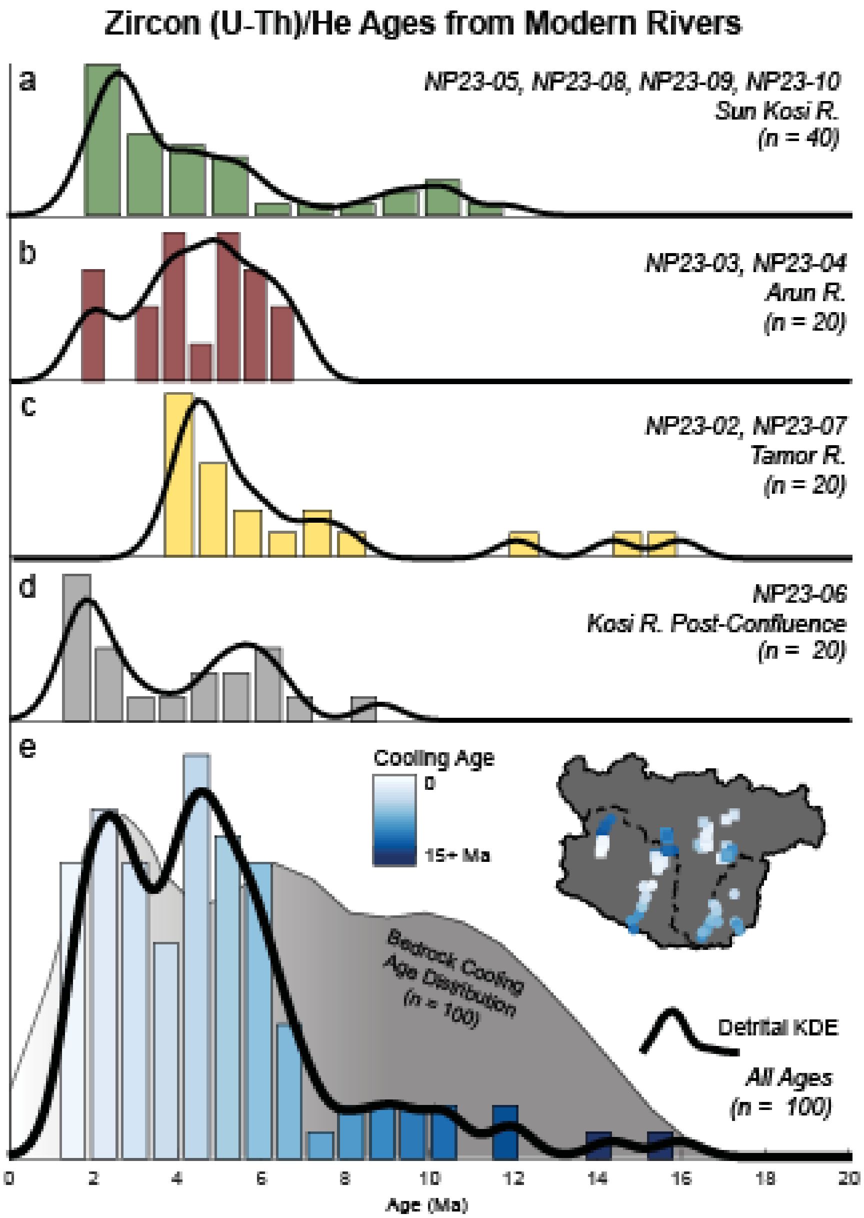

Figure 7. Low-temperature thermochronological age distributions by watershed. The singular 55 Ma grain from the Arun sample is removed for visualization purposes. (a) ZHe ages from Sun Kosi watershed samples (b) ZHe ages from Arun watershed samples (c) ZHe ages from Tamor watershed samples (d) ZHe ages from post-confluence sample (e) All detrital ZHe ages from this study. Histogram and bold KDE represent detrital grains, compared to bedrock ZHe

and ZFT combined age distribution in gray gradient. Inset watershed shows locations of bedrock ages.

To better understand detrital ZHe ages throughout the Kosi basin, we grouped ages by sub-watershed in addition to the full detrital age distribution (Table 2; Figure 7). Median ages by watershed are similar to each other and the overall distribution, ranging from 3.7 to 5.0 Ma. Median ages are not often applied to detrital studies as these datasets usually represent a distribution of ages derived from multiple sources. However, we use the median to emphasis where most grains fall within our age distributions and as a method for comparison to bedrock datasets. The youngest sub-population of ages is in the post-confluence sample, with seven grains younger than 2.0 Ma and a median age of 3.4 Ma. The age distribution from the Arun River is nearly unimodal, while Sun Kosi and Tamor age distributions are potentially multi-modal, with dominant ranges from 1.7 – 5.0 Ma and 7.0 – 12 Ma (Sun Kosi) and from 3.6 – 6.0 Ma and 12 – 16 Ma (Tamor; Figure 7).

Table 2. (U-Th)/He age ranges for each watershed, the post-confluence sample, and combined age distribution of all ages.

Composite Sample	**Number of Grains**	**Ages Present**	**Median Age**
Sun Kosi Watershed	40	1.7 ± 0.1 – 11.8 ± 0.2 Ma	3.7 Ma
Arun Watershed	20	1.7 ± 0.1 – 6.8 ± 0.1 Ma, with singular 55.2 ± 0.7 Ma outlier	4.9 Ma
Tamor Watershed	20	3.6 ± 0.1 – 15.9 ± 0.4 Ma	5.0 Ma
Post-Confluence	20	1.2 ± 0.1 – 8.8 ± 0.4 Ma	3.4 Ma
All Grains	100	1.2 ± 0.1 to 15.9 ± 0.4 Ma, with singular 55.2 ± 0.7 Ma outlier	4.4 Ma

There is some variability between samples within the same sub-watershed (Figure 5). Of the Sun Kosi samples, there is variation between samples taken from the main stem of the Sun Kosi and its tributaries. NP23-05 and NP23-09, both sampled from the main Sun Kosi River, show slight bimodality, with modes around ~2 Ma and ~10 Ma. NP23-08 (Dudh Kosi River) and NP23-10 (Tama Kosi River) report younger and more similar distributions, with modes around ~3 Ma and ~4 Ma, respectively. The upper Arun sample (NP23-04) is significantly older than the lower Arun sample (NP23-03). Most ages from the upper Arun fall between 4.9 – 6.8 Ma, while all ages from the lower sample are younger than 5.0 Ma. Both Tamor samples show similar ages, the only difference being a slightly more pronounced older age range (~13 – 16 Ma) for the upper sample (Figure 5). All individual ages by sample are reported in Supporting Information.

Zircon (U-Th)/He ages from published bedrock range from 1.4 to 17.0 Ma (Figure 3, Table 3). Ranges vary by tributary. Broadly, bedrock data show a similar range in age to our detrital datasets for each tributary and for the entire Kosi basin. However, the relative proportionality of ages within this range is skewed differently, with modern river detrital samples reporting younger median ages for each tributary and the full basin when compared to the associated bedrock ages.

Table 3. Reported zircon (U-Th)/He bedrock age ranges for each watershed and combined age distribution of all ages.

Composite Sample	**Number of Published Ages**	**Range of ZHe Ages Present**	**Median Age**
Sun Kosi Watershed	38	1.4 ± 0.25 – 16.1 ± 0.95 Ma	5.2 Ma
Arun Watershed	46	2.2 ± 0.06 – 17.0 ± 0.36 Ma	8.5 Ma
Tamor Watershed	17	5.4 ± 0.30 – 11.6 ± 0.50 Ma	7.9 Ma
Full Watershed	101	1.4 ± 0.02 – 17.0 ± 0.36Ma	7.6 Ma

4.3 Statistical Analyses: MDS and Mixture Model Results

We conducted two MDS analyses (Figure 8a-b) and two mixture models (Figure 8c-d) using our detrital zircon U-Pb data. The stress value using U-Pb age distributions by sample is poor (0.231; Figure 8a) and good when using composite watershed populations (0.041; Figure 8b) (Kruskal, 1964). The most similar individual sample age distributions to the post-confluence composite are the Tamor (NP23-02) and the upper Arun (NP23-04). The most similar samples to each other are the upper and lower Sun Kosi samples. The nearest neighbor watershed composite to the post-confluence sample is the Tamor, while the most similar distributions to each other by watershed are the Arun and Sun Kosi composites.

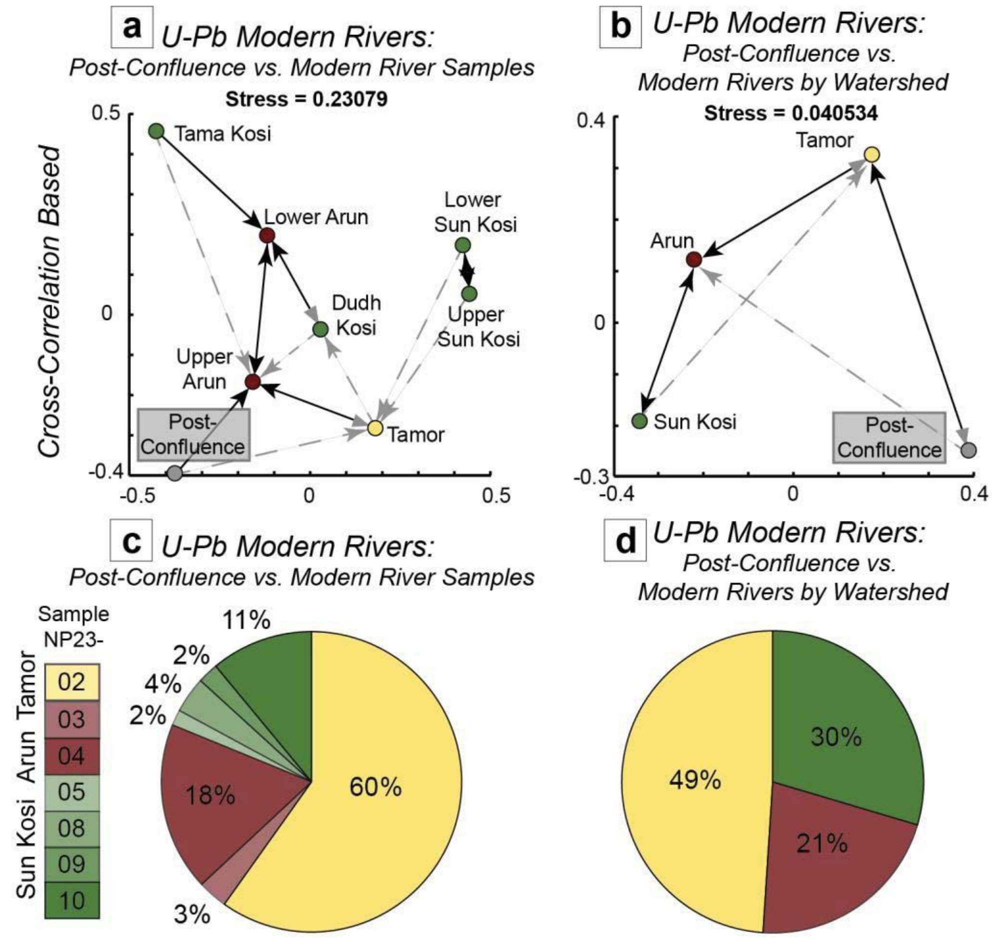

Figure 8. MDS analyses (a-b) and mixture model results (c-d) for U-Pb data (Supporting Information). Arrowheads point from each datapoint towards their first-nearest and second-nearest neighbors in solid black and dashed gray, respectively (a) Comparison of post-confluence U-Pb age distribution to all other individual modern river samples (b) Comparison of post-confluence U-Pb age distribution to composite U-Pb river sand distributions grouped by tributary watershed (c) Mixture model results of post-confluence U-Pb age distribution compared to individual modern river samples (d) Mixture model results of post-confluence U-

Pb age distribution compared to composite U-Pb river sand distributions grouped by tributary watershed

Mixture model results by sample show the Tamor sample (NP23-02) to be the largest contributor (60%) to the post-confluence region. Arun samples are modeled to contribute 21% and Sun Kosi samples are modeled to contribute 19%. By watershed, the Tamor remains the largest contributor (49%). MDS analyses and mixture models using bedrock composite distributions for the LHS, GHS, and THS/upper LHS as source populations are found in Supporting Information.

We additionally conducted two MDS analyses (Figure 9a-b) and two mixture models (Figure 9c-d) using our detrital ZHe data. The stress values for both analyses are fair (Figure 9a-b; Kruskal, 1964). MDS analysis for ZHe data shows the most similar sample to the post-confluence to be the upper Sun Kosi, followed by the lower Arun (Figure 9a-c). The most similar samples to each other are the upper Tamor and Tama Kosi. By watershed, the most similar composite to the post-confluence is the Sun Kosi, followed by the Arun, then the Tamor.

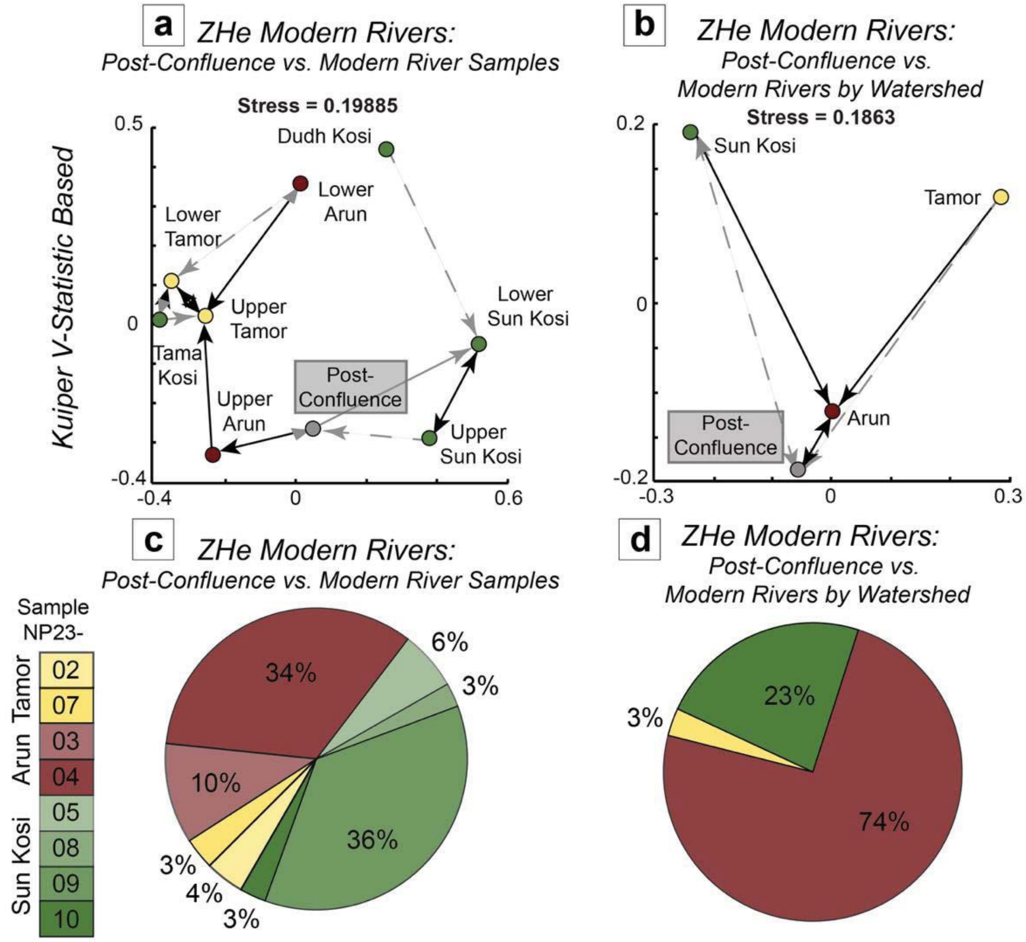

Figure 9. MDS analyses (a-b) and mixture model results (c-d) for ZHe data (Supporting Information). Arrowheads point from each datapoint towards their first-nearest and second-nearest neighbors in solid black and dashed gray, respectively (a) Comparison of post-confluence ZHe age distribution to all other individual modern river samples (b) Comparison of post-confluence ZHe age distribution to composite ZHe river sand distributions grouped by tributary watershed (c) Mixture model results of post-confluence ZHe age distribution compared to individual modern river samples (d) Mixture model results of post-confluence

ZHe age distribution compared to composite ZHe sand distributions grouped by tributary watershed

We use the Kuiper V-statistic to determine source contributions in our detrital ZHe dataset (Figure 9d-e). Mixture model results by sample show the Upper Sun Kosi (NP23-09) to be the largest contributor (36%), followed by the Upper Arun (NP34-04; 33%). When we run the mixing model by watershed, the Arun is the dominant contributor (74%), followed by the Sun Kosi (23%), and the Tamor (3%). This contrasts with mixing results from our geochronological dataset, which suggest the dominant contributor to be the Tamor. MDS analyses and mixture models using known bedrock cooling ages by watershed as source populations are found in Supporting Information.

5. Discussion

5.1 Geochronological Insights

Geochronologic results confirm sediment contribution from each major lithotectonic sequence by the point of sampling at the base of the watershed (Figure 6). Mixture models comparing tributary populations as potential sources to the post-confluence composite sample show considerable contributions from each tributary to the trunk river, thus demonstrating relatively equal contribution along strike. Our data also suggest that the dominant sediment source is the lower LHS, with additional prominent contributions from the GHS and intruding leucogranite bodies. Importantly, our river samples were collected during the current interglacial period and erosional regime, and interpretations are considered in this context.

The dominant U-Pb age range present in six of eight detrital samples is from 1700 – 2000 Ma (Figure 6; Table 1). This age range is characteristic of the lower LHS, which occupies the three tectonic windows in the Kosi watershed. We interpret that this consistent strong presence of LHS age grains in our detrital samples suggests a prominent contribution from those regions of the watershed. These Proterozoic ages also overlap with the 1600-1900 Ma age mode of the GHS and similar ages are present within the THS and upper LHS. Similarly, all samples contain variable quantities of zircon ages between ~400-700 Ma, an age mode not found in the LHS, but common in the GHS and THS/upper LHS. Based on the variable abundance of these ages, the data suggest the GHS and THS/upper LHS may be secondary but notable contributions. We note that, surprisingly, the 1700-2000 Ma population characteristic of the LHS, becomes less significant between the tributaries and the post-confluence samples, which instead show dominance of GHS and THS/upper LHS age populations. This may be due to natural variability, but the more subdued nature of the peak is recorded in both post-confluence samples. Recycling from GHS-derived zircons from the Siwalik Group (Baral et al., 2015) through which the post-confluence trunk river flows, may better explain the discrepancy between the tributaries and post-confluence data; this interpretation is supported by the increase in relative height of the ~1000 Ma peak between the upstream and downstream post-confluence sample as the river flows through an increasing stretch of Siwalik Group substrate.

We acknowledge the potential bias introduced when assuming that zircon budget is representative of sediment budget, as some studies have shown single mineral analysis to reflect bedrock fertility variability (e.g. Amidon et al., 2005a; Vezzoli et al., 2016). However, we note that some studies have shown LHS bedrock to have low zircon fertility, relative to the GHS and THS (e.g. Amidon et al., 2005b). Considering this, a strong contribution of zircon with an age population typical of the LHS is particularly noteworthy, as this bedrock source may be zircon poor relative to the other major contributing sources.

The presence of ~15-35 Ma zircon grains in all samples is indicative of erosion of mid-Miocene to latest Eocene leucogranites found within the GHS (Godin et al., 2001; Hodges, 2000; Lavé & Avouac, 2001). The relative lack of these age grains from the Tama Kosi (NP23-10), with only one grain, may reflect that this river system does not erode into a large, mapped leucogranite intrusion (Figure 3a). However, the Dudh Kosi (NP23-08) has 20 grains <50 Ma, reflecting the presence of leucogranites within its headwaters (Figure 3a). It is possible that the 8 grains between 35-50 Ma in the post-confluence sample may be sourced from the Siwalik Group at the base of the watershed, however these ages compose a small portion of the known age distributions of this group (Baral et al., 2015). With these inferences in mind, we interpret these young U-Pb ages to further support a region of erosion in parts of the GHS portions of the watershed. Although characteristic bedrock spectra between the GHS and the THS/upper LHS are similar and thus provenance discrimination between them is difficult, we suggest all samples also reflect detrital U-Pb age ranges associated with the THS and upper LHS bedrock age distribution. Our U-Pb age populations from the Arun (NP23-03, -04) contain a scattering (n = 7/465) of grains between 25 Ma and 37 Ma with elevated U/Th that support derivation from the Tethyan Himalaya leucogranites (Supporting Information). In addition, these samples contain several grains (n = 10/465) with U-Pb ages between 44 Ma and 140 Ma with U/Th ratios <50, which may be derived from the suture zone assemblages (Supporting Information). We consider the presence of these ages to support some sediment contribution from the THS. However, we are cautious to use the presence of THS and upper LHS ages to identify the spatial focus of erosion as these units occupy both the southernmost and northernmost areas of the basin. This lack of spatial resolution was further reflected when conducting quantitative models using bedrock age distributions as potential sources (Supporting Information). We found that bedrock based mixture models were not fruitful in targeting dominant sediment sources, due to the geographic extent of the THS and upper LHS bedrock. These qualitative and quantitative observations highlight the inability of detrital zircon U-Pb geochronology to determine the spatial focus of erosion within the Kosi watershed without a secondary routing metric such as low-temperature thermochronology.

5.2 Thermochronological Insights

Thermochronological results suggest a dominant detrital signal from rocks with the youngest bedrock cooling ages in the watershed. Modern river sands yield consistently younger (4.4 Ma) ZHe cooling ages in comparison with the published bedrock record (7.6 Ma; Tables 1 and 2). Based on the location of young bedrock cooling ages, we correlate this range of young ages, <6 Ma, to the center of the watershed by latitude. This places the dominant band of erosion during the modern interglacial period near the “High Himalaya Topographic Front” (Whipple et al. 2023; Figure 2c) and broadly in agreement with the dominant region of erosion reported by Johnston et al. (2020), in a similar study along strike. In addition, the young cooling ages spatially overlap with the LHS and GHS, including <33 Ma leucogranite intrusions of the GHS as compared to the ~33-45 Ma leucogranites that are more characteristic of the THS and upper LHS (Cao et al., 2022). Thus, the ZHe data allow us to refine interpretations from the U-Pb analysis, where there is similarity in Cambrian-Neoproterozoic and Mesoproterozoic-Paleoproterozoic age modes between the GHS and THS and upper LHS. While 99/100 grains in our dataset record ages younger than 16 Ma, we discuss possible explanations for the presence of a singular 55 Ma grain from the upper Arun (NP23-04) in Supporting Information.

Our detrital ZHe dataset also allows us to evaluate the merits of using this method as a provenance indicator. We find that statistical interpretations of our thermochronological dataset are limited by two main factors: spatial bias and small sample size. This study has the benefit of being conducted in one of the most well-researched basins in the world yet remains biased by bedrock data availability. Geologic studies by nature tend to be conducted in areas of geologic interest, likely biasing these data to overrepresent areas with unique cooling signatures. For example, the Arun bedrock dataset includes a large portion of bedrock ages studying recent exhumation by Tibetan normal faults (e.g., Jessup et al., 2008; McDermott, 2012). Bedrock data in the Sun Kosi region, alternatively, are largely sourced from consistent N-S traverses, offering a more uniform understanding of cooling age along strike (e.g., Nakajima et al., 2020; Wang et al., 2010). We suggest that this inconsistency limits the utility of bedrock-based mixture modeling using ZHe data. Therefore, as with our U-Pb dataset, we found that quantitative mixture and MDS models using the bedrock records were not fruitful in our analysis (Supporting Information).

As a further limitation, low-temperature thermochronological analysis is an expensive and time-consuming method. We find that this small-n dataset allows for qualitative analysis but is limited in quantitative analysis as mixture models are most robust with a large-n dataset (Sundell & Saylor, 2017). Our mixture model results highlight the potential issues that arise using a small-n dataset. For example, we find a stark contrast in ZHe mixture results when conducting the model using individual samples (Figure 9c) compared to by sub-watershed (Figure 9d). Primarily, this is articulated by a 30% increase in sediment contribution from the Arun when conducting our model by sub-watershed (44% contribution from individual Arun samples compared to 74% by watershed). We do not see this same discrepancy in our U-Pb dataset, with the largest contribution difference between individual sample models and sub-watershed models being 11% (Figure 8c-d). We take these results to caution against exclusively using absolute mixing values from quantitative analysis. However, we argue there is still value in considering the qualitative takeaways from these mixture models.

5.3 Benefits of a Dual-Proxy Approach

Our results show that by considering dating metric results together, we are able to better constrain the dominant region of erosion in a structurally complex basin. Both approaches of using zircon U-Pb geochronology and (U-Th)/He thermochronology present the same broad conclusions, that sediment in the Kosi basin is dominantly sourced from the central basin. U-Pb results suggest a dominant sediment contribution from the lower LHS tectonic windows, the GHS, and leucogranite intrusions. ZHe results suggest dominant sediment contribution from regions with the youngest thermochronologic cooling signature. Integrating these datasets, we confine sediment in the Kosi basin to be primarily derived from the northern regions of the tectonic windows and the southern portion of GHS (Supporting Information). This focus correlates with models of highest erosion rates (e.g., Whipple et al., 2023; Figure 2D).

5.4 Disagreement with Climatically Driven Landscape Evolution

Integrating our datasets, we interpret the focus of erosion within the Kosi watershed to be from the northern section of the LHS windows into the GHS (Figure 10). Within the context of the modern interglacial period, this region is north of the heaviest precipitation band and south of the most glaciated areas in the basin (Figure 10a; Funk et al. 2015; GLIMS Consortium, 2005).

We argue that if present-day landscape change was driven exclusively by climatic factors, our detrital sediment signal would be reflective of geochronologic and thermochronologic ages that are characteristic of the bedrock in one or both of these regions. For example, we would expect erosion from glacial retreat in the high Himalaya to predict a greater contribution of ZHe dates older than 10 Ma than observed in our data (7 grains out of 100) (e.g., Orme et al., 2015; Schulz, 2017; Streule et al., 2012). Figure 10a highlights the spatial disagreement between precipitation, glaciation, and detrital sediment signal. This discrepancy emphasizes the need for some additional driver beyond climate to influence landscape evolution in the basin. Below we outline these potential drivers, while addressing the limitations of our study to test for the effects of localized climatically driven erosion processes such as landslides and glacial outburst floods.

5.5 Structural Implications

We argue that our identified dominant erosion band coincides with inferred structures at depth, interpreting our results to support a model of landscape evolution in the Kosi basin in which the Main Himalayan Thrust at depth plays a role in shaping the topographic landscape (Figure 10b). Using a similar method along strike in central Nepal, Johnston et al. (2020) find peak erosion in the Marsyandi basin to also be located just north of the MCT and overlapping with proposed locations of the Main Himalayan Thrust ramp. When comparing this dominant erosive signal to studies constraining ramp geometry at depth (e.g., Hubbard et al., 2016; Elliot et al., 2016), they conclude that significant duplexing on a midcrustal ramp 80 – 100 km north of the MFT is required to fit their data to these geometries. We interpret our data to support a similar tectonic geometry signal across strike due to consistency in the dominant detrital signal across all three sub-basins in the Kosi watershed.

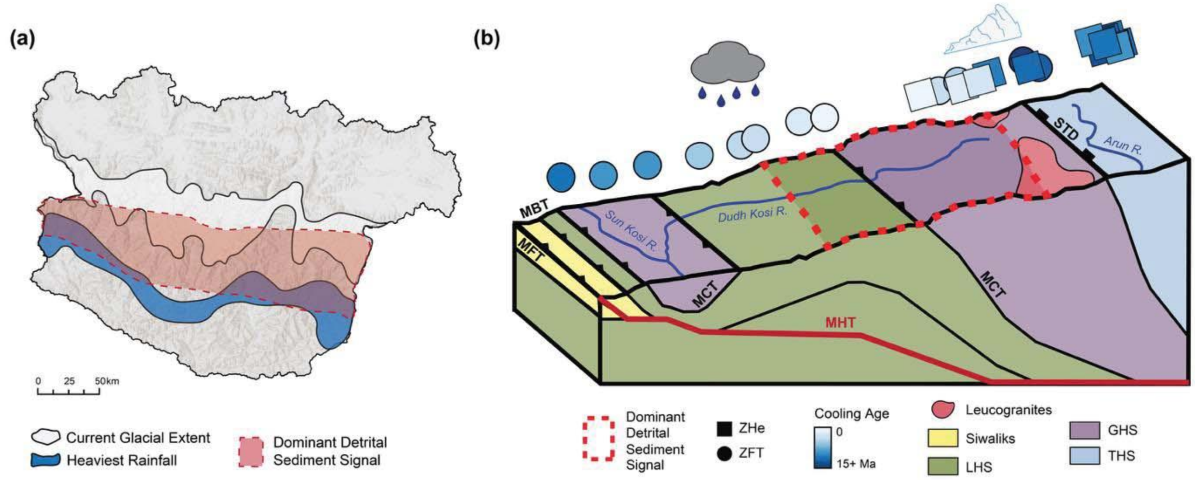

Figure 10. (a) Generalized tracing of dominant sediment signal from this study compared to band of heaviest rainfall and current glacial extent (Funk et al., 2015; GLIMS Consortium, 2005) (b) Schematic cross-section highlighting location of dominant sediment signal in reference to surface geology, structure, and climatic signals. Structure at depth modified from Hubbard et al. (2016). Thermochronological symbols represent bedrock ages along Dudh Kosi river profile within ~50 km (Figure 3). Raincloud represents approximate latitude of highest precipitation and glacial graphic represents approximate latitude of glaciation.

This interpretation further agrees with the other studies along strike investigating geometric structure at depth, which emphasize the need for internal deformation to explain surface observations of topography and thermochronometry (e.g., Johnston et al., 2020; McQuarrie et al., 2014; Sherpa et al., 2024; K. Whipple et al., 2016). For our schematic cross-section (Figure 10b), we incorporate a cross-section proposed by Hubbard et al. (2016) in light of the 2015 Gorkha earthquake. This model includes a series of three deep ramps within the MHT, producing an imbricated duplex. Our interpreted region of dominant sedimentation falls above of this ramp structure at depth, supporting this model.

Our results further agree with the peak erosive band proposed for the Arun watershed by Olen et al. (2015). This study, using ^{10}Be to determine denudation rates, also argues for a strong tectonic forcing signal, in agreement with studies such as Godard et al. (2012) and Burbank et al. (2003), citing similar denudation patterns in the Arun valley and in studies where denudation rates are fit to tectonic drivers (Olen et al., 2015). Importantly, however, Olen et al. (2015) also acknowledge the limitations of their detrital dataset, specifically in the inability to rule out climatic influences such as glaciation and localized landslides. The resolution of our data also does not allow us to tease out these signals. One could possibly test for the influence of these signals by focusing the study area closer to these processes in the higher elevations of the Himalaya or by sampling before and after significant landslide events. In addition, Olen et al. (2015) note the possibility of a diluted Tibetan signal due to the washing out of larger grains (e.g., >2 mm) analyzed in their detrital dataset by the point of sampling. This limitation is also possible in our dataset, especially in consideration of the presence of a singular ZHe 55 Ma grain , which is likely derived from Tibet (Dai et al. 2013; Lee et al. 2009). However, in agreement with this study, we ultimately argue that our detrital data is broadly representative of the sediment profile in the Kosi River, thus providing a useful tool for investigating landscape evolution in this system.

6.0 Summary

By combining geochronological and thermochronological methods, we are able to better isolate the dominant detrital sediment signal in the Kosi basin to its mid-latitudes and mid-elevations (Figure 10a). U-Pb data supports that sediment is dominantly sourced from the lower LHS owing to the consistent 1700-2000 Ma age mode, but contributions from the GHS and THS/upper LHS are more challenging to resolve. ZHe data supports that sediment is dominantly sourced from the youngest cooling ages in the watershed, which are found within the LHS and GHS. Integrated, these signals isolate a band of focused erosion and support the hypothesis that tectonics, not exclusively climatic factors, continue to play a key role in shaping the landscape in the region during the modern interglacial period. While our data does not explicitly allow for distinction of a particular tectonic model, nor does it rule out the role of high slope topography, it supports a model in which duplexing along a midcrustal ramp at depth continues to provide rock to be eroded at the surface, in agreement with studies advocating for a prominent tectonic forcer in landscape evolution (e.g., Godard et al., 2012; Johnston et al., 2020).

Acknowledgements: This work was supported by NSF-EAR-NERC Award #2026870 to D.A. Orme. We are grateful for the organizational skills and friendship of Bhairab Satula in facilitating field work in Nepal. We thank Victor Valenica at ZirChron LLC for mineral separation and are grateful for Jim Metcalf at the CU TRAILS lab for his work on zircon (U-Th)/He analyses. We thank the staff at The University of Arizona LaserChron Center for their work on zircon U-Pb analyses (NSF-EAR 2050246). We appreciate two anonymous reviewers, Associate Editor Yuntao Tian, and Editor Taylor Schildgen for their time and effort to review, improve, and handle this manuscript.

Open Research

Data Availability Statement

The zircon U-Pb and zircon (U-Th)/He data presented in this study are available through open access of this article. See 2025TC009035-sup0002-TableSI-S01 for U-Pb data. See 2025TC009035-sup0003-TableSI-S02 for (U-Th)/He data.

Conflict of Interest Statement

The authors have no conflicts of interest to disclose.

References

Amidon, W., Burbank, D., & Gehrels, G. (2005a). U–Pb zircon ages as a sediment mixing tracer in the Nepal Himalaya. *Earth and Planetary Science Letters*, *235*(1–2), 244–260. https://doi.org/10.1016/j.epsl.2005.03.019

Amidon, W. H., Burbank, D. W., & Gehrels, G. E. (2005b). Construction of detrital mineral populations: Insights from mixing of U–Pb zircon ages in Himalayan rivers. *Basin Research*, *17*(4), 463–485. https://doi.org/10.1111/j.1365-2117.2005.00279.x

Argand, E. (1924). *La tectonique de 1'Asie*. *Int. Geol Congr.* 13(1), 170–372.

Baral, U., Lin, D., & Chamlagain, D. (2016). Detrital zircon U–Pb geochronology of the Siwalik Group of the Nepal Himalaya: Implications for provenance analysis. *International Journal of Earth Sciences*, *105*(3), 921–939. https://doi.org/10.1007/s00531-015-1198-7

Beaumont, C., Fullsack, P., & Hamilton, J. (1992). Erosional control of active compressional orogens. In K. R. McClay (Ed.), *Thrust Tectonics*, 1–18. Springer Netherlands. https://doi.org/10.1007/978-94-011-3066-0_1

Blum, M., & Pecha, M. (2014). Mid-Cretaceous to Paleocene North American drainage reorganization from detrital zircons. *Geology*, *42*(7), 607–610. https://doi.org/10.1130/G35513.1

Bookhagen, B., & Burbank, D. W. (2010). Toward a complete Himalayan hydrological budget: Spatiotemporal distribution of snowmelt and rainfall and their impact on river discharge. *Journal of Geophysical Research: Earth Surface*, *115*(F3). https://doi.org/10.1029/2009JF001426

Burbank, D. W., Blythe, A. E., Putkonen, J., Pratt-Sitaula, B., Gabet, E., Oskin, M., Barros, A., & Ojha, T. P. (2003). Decoupling of erosion and precipitation in the Himalayas. *Nature*, *426*(6967), 652–655. https://doi.org/10.1038/nature02187

Cao, H. W., Pei, Q. M., Santosh, M., Li, G. M., Zhang, L. K., Zhang, X. F., Zhang, Y. H., Zou, H., Dai, Z. W., Lin, B., Tang, L., & Yu, X. (2022). Himalayan leucogranites: A review of geochemical and isotopic characteristics, timing of formation, genesis, and rare metal mineralization. *Earth-Science Reviews*, *234*, 104229. https://doi.org/10.1016/j.earscirev.2022.104229

Carrapa, B., Faiz Bin Hassim, M., Kapp, P. A., DeCelles, P. G., & Gehrels, G. (2017). Tectonic and erosional history of southern Tibet recorded by detrital chronological signatures along the Yarlung River drainage. *Geological Society of America Bulletin*, *129*(5–6), 570–581. https://doi.org/10.1130/B31587.1

Chapman, J. B., & Kapp, P. (2017). Tibetan Magmatism Database. *Geochemistry, Geophysics, Geosystems*, *18*(11), 4229–4234. https://doi.org/10.1002/2017GC007217

Clift, P. D., & Webb, A. A. G. (2019). A history of the Asian monsoon and its interactions with solid Earth tectonics in Cenozoic South Asia. *Geological Society, London, Special Publications*, *483*(1), 631–652.

Clift, P. D., & Jonell, T. N. (2021). Monsoon controls on sediment generation and transport: Mass budget and provenance constraints from the Indus River catchment, delta and submarine fan over tectonic and multimillennial timescales. *Earth-Science Reviews*, *220*, 103682. https://doi.org/10.1016/j.earscirev.2021.103682

Colleps, C. L., McKenzie, N. R., Stockli, D. F., Hughes, N. C., Singh, B. P., Webb, A. A. G., Myrow, P. M., Planavsky, N. J., & Horton, B. K. (2018). Zircon (U-Th)/He Thermochronometric Constraints on Himalayan Thrust Belt Exhumation, Bedrock Weathering, and Cenozoic Seawater Chemistry. *Geochemistry, Geophysics, Geosystems*, *19*, 257–271.

Dai, J., Wang, C., Hourigan, J., Li, Z., & Zhuang, G. (2013). Exhumation history of the Gangdese batholith, southern Tibetan Plateau: Evidence from apatite and zircon (U-Th)/He thermochronology. *The Journal of Geology*, *121*(2), 155-172.

Dal Zilio, L., Van Dinther, Y., Gerya, T., & Avouac, J. P. (2019). Bimodal seismicity in the Himalaya controlled by fault friction and geometry. *Nature Communications*, *10*(1), 48. https://doi.org/10.1038/s41467-018-07874-8

DeCelles, P. G., Carrapa, B., Ojha, T. P., Gehrels, G. E., & Collins, D. (2020). Structural and Thermal Evolution of the Himalayan Thrust Belt in Midwestern Nepal. In P. G. DeCelles, B. Carrapa, T. P. Ojha, G. E. Gehrels, & D. Collins, *Structural and Thermal Evolution of the Himalayan Thrust Belt in Midwestern Nepal* (pp.1–79). Geological Society of America. https://doi.org/10.1130/2020.2547(01)

DeCelles, P. G., Gehrels, G. E., Quade, J., & Ojha, T. P. (1998). Eocene-early Miocene foreland basin development and the history of Himalayan thrusting, western and central Nepal. *Tectonics*, *17*(5), 741–765. https://doi.org/10.1029/98TC02598

DeCelles, P. G., Robinson, D. M., Quade, J., Ojha, T. P., Garzione, C. N., Copeland, P., & Upreti, B. N. (2001). Stratigraphy, structure, and tectonic evolution of the Himalayan fold-thrust belt in western Nepal. *Tectonics*, *20*(4), 487–509. https://doi.org/10.1029/2000TC001226

Dhital, M. R. (2015). Lesser Himalaya of Koshi Region. In M. R. Dhital, *Geology of the Nepal Himalaya* (pp. 163–177). Springer International Publishing. https://doi.org/10.1007/978-3-319-02496-7_11

Dodson, M. H. (1973). Closure temperature in cooling geochronological and petrological systems. *Contributions to Mineralogy and Petrology*, *40*(3), 259–274. https://doi.org/10.1007/BF00373790

Elliott, J. R., Jolivet, R., González, P. J., Avouac, J. P., Hollingsworth, J., Searle, M. P., & Stevens, V. L. (2016). Himalayan megathrust geometry and relation to topography revealed by the Gorkha earthquake. *Nature Geoscience*, *9*(2), 174–180. https://doi.org/10.1038/ngeo2623

Flowers, R. M., Zeitler, P. K., Danišík, M., Reiners, P. W., Gautheron, C., Ketcham, R. A., Metcalf, J. R., Stockli, D. F., Enkelmann, E., & Brown, R. W. (2023). (U-Th)/He chronology: Part 1. Data, uncertainty, and reporting. *Bulletin*, *135*(1–2), 104–136.

Funk, C., Peterson, P., Landsfeld, M., Pedreros, D., Verdin, J., Shukla, S., Husak, G., Rowland, J., Harrison, L., Hoell, A., & Michaelsen, J. (2015). The climate hazards infrared precipitation with stations—A new environmental record for monitoring extremes. *Scientific Data*, *2*(1), 150066. https://doi.org/10.1038/sdata.2015.66

Gehrels, G. (2014). Detrital Zircon U-Pb Geochronology Applied to Tectonics. *Annual Review of Earth and Planetary Sciences*, *42*(1), 127–149. https://doi.org/10.1146/annurev-earth-050212-124012

Gehrels, G., Kapp, P., DeCelles, P., Pullen, A., Blakey, R., Weislogel, A., Ding, L., Guynn, J., Martin, A., McQuarrie, N., & Yin, A. (2011). Detrital zircon geochronology of pre-Tertiary strata in the Tibetan-Himalayan orogen. *Tectonics*, *30*(5). https://doi.org/10.1029/2011TC002868

Gehrels, G., Valencia, V., & Ruiz, J. (2008). Enhanced precision, accuracy, efficiency, and spatial resolution of U-Pb ages by laser ablation–multicollector–inductively coupled plasma–mass spectrometry. *Geochemistry, Geophysics, Geosystems*, *9*(3).

Gemignani, L., Van Der Beek, P. A., Braun, J., Najman, Y., Bernet, M., Garzanti, E., & Wijbrans, J. R. (2018). Downstream evolution of the thermochronologic age signal in the Brahmaputra catchment (eastern Himalaya): Implications for the detrital record of erosion. *Earth and Planetary Science Letters*, *499*, 48–61. https://doi.org/10.1016/j.epsl.2018.07.019

GLIMS Consortium. (2005). *GLIMS Glacier Database, Version 1* [Dataset]. ASA National Snow and Ice Data Center Distributed. Active Archive Center. https://doi.org/10.7265/N5V98602

Godard, V., Bourlès, D. L., Spinabella, F., Burbank, D. W., Bookhagen, B., Fisher, G. B., Moulin, A., & Léanni, L. (2014). Dominance of tectonics over climate in Himalayan denudation. *Geology*, *42*(3), 243–246. https://doi.org/10.1130/G35342.1

Godard, V., Burbank, D. W., Bourlès, D. L., Bookhagen, B., Braucher, R., & Fisher, G. B. (2012). Impact of glacial erosion on ^{10}Be concentrations in fluvial sediments of the

Marsyandi catchment, central Nepal. *Journal of Geophysical Research: Earth Surface*, *117*(F3), 2011JF002230. https://doi.org/10.1029/2011JF002230

Godin, L., Parrish, R. R., Brown, R. L., & Hodges, K. V. (2001). Crustal thickening leading to exhumation of the Himalayan Metamorphic core of central Nepal: Insight from U-Pb Geochronology and ^{40}Ar/^{39}Ar Thermochronology. *Tectonics*, *20*(5), 729–747. https://doi.org/10.1029/2000TC001204

Grandin, R., Doin, M. P., Bollinger, L., Pinel-Puyssegur, B., Ducret, G., Jolivet, R., & Sapkota, S. N. (2012). Long-term growth of the Himalaya inferred from interseismic InSAR measurement. *Geology*, *40*(12), 1059–1062. https://doi.org/10.1130/G33154.1

Guenthner, W. R., Reiners, P. W., Ketcham, R. A., Nasdala, L., & Giester, G. (2013). Helium diffusion in natural zircon: Radiation damage, anisotropy, and the interpretation of zircon (U-Th)/He thermochronology. *American Journal of Science*, *313*(3), 145–198. https://doi.org/10.2475/03.2013.01

Gupta, N., & Tandon, S. K. (Eds.). (2020). *Geodynamics of the Indian Plate: Evolutionary Perspectives*. Springer International Publishing. https://doi.org/10.1007/978-3-030-15989-4

Han, X., Dai, J. G., Smith, A. G. G., Xu, S. Y., Liu, B. R., Wang, C. S., & Fox, M. (2024). Recent uplift of Chomolungma enhanced by river drainage piracy. *Nature Geoscience*, *17*(10), 1031–1037. https://doi.org/10.1038/s41561-024-01535-w

He, J. J. Y. and Reiners, P. W. (2002). A revised alpha-ejection correction calculation for (U–Th)/He thermochronology dates of broken apatite crystals. *Geochronology,* 4, 629–640, https://doi.org/10.5194/gchron-4-629-2022, 2022.

Heri, A., Aitchison, J., King, J., & Villa, I. (2015). Geochronology and isotope geochemistry of Eocene dykes intruding the Ladakh Batholith. *Lithos*, *212*, 111–121. https://doi.org/10.1016/j.lithos.2014.11.001

Hodges, K., Bowring, S., Davidek, K., Hawkins, D., & Krol, M. (1998). Evidence for rapid displacement on Himalayan normal faults and the importance of tectonic denudation in the evolution of mountain ranges. *Geology*, *26*(6), 483. https://doi.org/10.1130/0091-7613(1998)026<0483:EFRDOH>2.3.CO;2

Hodges, K. V. (2000). Tectonics of the Himalaya and southern Tibet from two perspectives. *Geological Society of America Bulletin*, 112(3), 324-350.

Hodges, K. V., Hurtado, J. M., & Whipple, K. X. (2001). Southward extrusion of Tibetan crust and its effect on Himalayan tectonics. *Tectonics*, *20*(6), 799–809. https://doi.org/10.1029/2001TC001281

Huang, F., Xu, J., Zeng, Y., Chen, J., Wang, B., Yu, H., Huang, W., & Tan, R. (2017). Slab breakoff of the Neo-Tethys Ocean in the Lhasa Terrane inferred from contemporaneous melting of the mantle and crust. *Geochemistry, Geophysics, Geosystems*, *18*, 4074–4095. https://doi.org/10.1002/2017GC007039

Hubbard, J., Almeida, R., Foster, A., Sapkota, S. N., Bürgi, P., & Tapponnier, P. (2016). Structural segmentation controlled the 2015 Mw 7.8 Gorkha earthquake rupture in Nepal. *Geology*, *44*(8), 639–642. https://doi.org/10.1130/G38077.1

Huntington, K. W., Blythe, A. E., & Hodges, K. V. (2006). Climate change and Late Pliocene acceleration of erosion in the Himalaya. *Earth and Planetary Science Letters*, *252*(1–2), 107–118. https://doi.org/10.1016/j.epsl.2006.09.031

Huntington, K. W., & Hodges, K. V. (2006). A comparative study of detrital mineral and bedrock age-elevation methods for estimating erosion rates. *Journal of Geophysical Research: Earth Surface*, *111*(F3). https://doi.org/10.1029/2005JF000454.

Huyghe, P., Bernet, M., Galy, A., Naylor, M., Cruz, J., Gyawali, B.R., Gemingani, L., Mugnier, J-L. (2020). Rapid exhumation since at least 13 Ma in the Himalaya recorded by detrital apatite fission-track dating of Bengal fan (IODP Expedition 354) and modern Himalayan river sediments. *Earth and Planetary Sciences Letters, 534.* https://doi.org/10.1016/j/epsl.2020.116078.

Ibañez-Mejia, M., Pullen, A., Pepper, M., Urbani, F., Ghoshal, G., & Ibañez-Mejia, J. C. (2018). Use and abuse of detrital zircon U-Pb geochronology—A case from the Río Orinoco delta, eastern Venezuela. *Geology*. https://doi.org/10.1130/G45596.1

Jessup, M. J., Newell, D. L., Cottle, J. M., Berger, A. L., & Spotila, J. A. (2008). Orogen-parallel extension and exhumation enhanced by denudation in the trans-Himalayan Arun River gorge, Ama Drime Massif, Tibet-Nepal. *Geology*, *36*(7), 587-590. https://doi.org/10.1130/G24722A.1

Johnston, S. N., Cannon, J. M., & Copeland, P. (2020). Post-Miocene Erosion in Central Nepal Controlled by Midcrustal Ramp Position, Duplex Growth, and Dynamically Maintained Elastic Strain. *Tectonics*, *39*(12), e2020TC006291. https://doi.org/10.1029/2020TC006291

Kapp, P., & DeCelles, P. G. (2019). Mesozoic–Cenozoic geological evolution of the Himalayan-Tibetan orogen and working tectonic hypotheses. *American Journal of Science*, *319*(3), 159–254. https://doi.org/10.2475/03.2019.01

Kennett, J. P. (1977). Cenozoic evolution of Antarctic glaciation, the circum-Antarctic Ocean, and their impact on global paleoceanography. *Journal of Geophysical Research*, *82*(27), 3843–3860. https://doi.org/10.1029/JC082i027p03843

Khadka, M., Kayastha, R. B., & Kayastha, R. (2020). Future projection of cryospheric and hydrologic regimes in Koshi River basin, Central Himalaya, using coupled glacier dynamics and glacio-hydrological models. *Journal of Glaciology*, *66*(259), 831–845. https://doi.org/10.1017/jog.2020.51

Kruskal, J. B. (1964). Multidimensional scaling by optimizing goodness of fit to a nonmetric hypothesis. *Psychometrika*, *29*(1), 1–27.

Lavé, J., & Avouac, J. P. (2001). Fluvial incision and tectonic uplift across the Himalayas of central Nepal. *Journal of Geophysical Research: Solid Earth*, *106*(B11), 26561–26591. https://doi.org/10.1029/2001JB000359

Lawver, L. A., & Gahagan, L. M. (1998). Opening of drake passage and its impact on Cenozoic Ocean circulation. *Oxf Monogr Biogeogr*, *39*, 212–226.

Lee, H. Y., Chung, S. L., Lo, C. H., Ji, J., Lee, T. Y., Qian, Q., & Zhang, Q. (2009). Eocene Neotethyan slab breakoff in southern Tibet inferred from the Linzizong volcanic record. *Tectonophysics*, *477*(1-2), 20-35.

Lindsey, E. O., Almeida, R., Mallick, R., Hubbard, J., Bradley, K., Tsang, L. L. H., et al. (2018). Structural control on downdip locking extent of the Himalayan megathrust. *Journal of Geophysical Research: Solid Earth*, 123, 5265–5278.

Link, P. K., Welcker, C. W., & Sundell, K. E. (2023). The geochronometry of Idaho and the bumpy barcode revisited: Snake River detrital zircons in Hells Canyon and beyond. *Sedimentary Geology*, *456*, 106497. https://doi.org/10.1016/j.sedgeo.2023.106497

Long, S. P., McQuarrie, N., Tobgay, T., Coutand, I., Cooper, F. J., Reiners, P. W., Wartho, J., & Hodges, K. V. (2012). Variable shortening rates in the eastern Himalayan thrust belt, Bhutan: Insights from multiple thermochronologic and geochronologic data sets tied to kinematic reconstructions. *Tectonics*, *31*(5), 2012TC003155. https://doi.org/10.1029/2012TC003155

McDermott, J. A. (2012). *Plio-Pleistocene North-South and East-West Extension at the Southern Margin of the Tibetan Plateau*. [Doctoral dissertation, Arizona State University].

McDermott, J. A., Whipple, K., Hodges, K. V., & van Soest, M. C. (2013). Evidence for Plio-Pleistocene north-south extension at the southern margin of the Tibetan Plateau, Nyalam region. *Tectonics*, *32*(3), 317–333. https://doi.org/10.1002/tect.20018

McQuarrie, N., Tobgay, T., Long, S. P., Reiners, P. W., & Cosca, M. A. (2014). Variable exhumation rates and variable displacement rates: Documenting recent slowing of Himalayan shortening in western Bhutan. *Earth and Planetary Science Letters*, *386*, 161–174. https://doi.org/10.1016/j.epsl.2013.10.045

Metcalf, K., & Kapp, P. (2019). History of subduction erosion and accretion recorded in the Yarlung Suture Zone, southern Tibet. *Geological Society, London, Special Publications*, *483*(1), 517–554. https://doi.org/10.1144/SP483.12

Molnar, P., & England, P. (1990). Late Cenozoic uplift of mountain ranges and global climate change: Chicken or egg? *Nature*, *346*(6279), 29–34. https://doi.org/10.1038/346029a0

Murphy, M. A., & Mark Harrison, T. (1999). Relationship between leucogranites and the Qomolangma detachment in the Rongbuk Valley, south Tibet. *Geology*, *27*(9), 831. https://doi.org/10.1130/0091-7613(1999)027<0831:RBLATQ>2.3.CO;2

Nakajima, T., Kawakami, T., Iwano, H., Danhara, T., & Sakai, H. (2022). Denudation Process of Crystalline Nappes in a Continental Collision Zone Constrained by Inversion of Fission-Track Data and Thermokinematic Forward Modeling: An Example From Eastern Nepalese Himalaya. *Journal of Geophysical Research: Solid Earth*, *127*(5), e2021JB023630. https://doi.org/10.1029/2021JB023630

Nakajima, T., Sakai, H., Iwano, H., Danhara, T., & Hirata, T. (2020). Northward younging zircon fission-track ages from 13 to 2 Ma in the eastern extension of the Kathmandu nappe and underlying Lesser Himalayan sediments distributed to the south of Mt. Everest. *Island Arc*, *29*(1), e12352. https://doi.org/10.1111/iar.12352

Nicholls, R. J., Hutton, C. W., Adger, W. N., Hanson, S. E., Rahman, Md. M., & Salehin, M. (Eds.). (2018). *Ecosystem Services for Well-Being in Deltas: Integrated Assessment for Policy Analysis*. Springer International Publishing. https://doi.org/10.1007/978-3-319-71093-8

Olen, S. M., Bookhagen, B., Hoffmann, B., Sachse, D., Adhikari, D. P., & Strecker, M. R. (2015). Understanding erosion rates in the Himalayan orogen: A case study from the Arun Valley. *Journal of Geophysical Research: Earth Surface*, *120*(10), 2080–2102. https://doi.org/10.1002/2014JF003410

Orme, D. A., Reiners, P. W., Hourigan, J. K., & Carrapa, B. (2015). Effects of inherited cores and magmatic overgrowths on zircon (U-Th)/He ages and age-eU trends from Greater Himalayan sequence rocks, Mount Everest region, Tibet. *Geochemistry, Geophysics, Geosystems*, *16*(8), 2499–2507. https://doi.org/10.1002/2015GC005818

Parkash, B., Sharma, R. P., & Roy, A. K. (1980). The Siwalik group (Molasse)—Sediments shed by collision of continental plates. *Sedimentary Geology*, *25*(1–2), 127–159. https://doi.org/10.1016/0037-0738(80)90058-5

Parrish, R. R., & Hodges, K. V. (1996). Isotopic constraints on the age and provenance of the Lesser and Greater Himalayan sequences, Nepalese Himalaya. *Geological Society of America Bulletin*, *108*(7), 904–911. https://doi.org/10.1130/0016-7606(1996)108<0904:ICOTAA>2.3.CO;2

Peyton, S. L., & Carrapa, B. (2013). An Introduction to Low-temperature Thermochronologic Techniques, Methodology, and Applications. In C. N. Knight, J. J. Cuzella, & L. D. Cress, *Application of Structural Methods to Rocky Mountain Hydrocarbon Exploration and Development*. American Association of Petroleum Geologists. https://doi.org/10.1306/13381688St653578

Pullen, A., Ibáñez-Mejía, M., Gehrels, G. E., Ibáñez-Mejía, J. C., & Pecha, M. (2014). What happens when n= 1000? Creating large-n geochronological datasets with LA-ICP-MS for geologic investigations. *J. Anal. At. Spectrom.*, *29*(6), 971–980. https://doi.org/10.1039/C4JA00024B

Rahl, J.M., Reiners, P.W., Campbell, I.H., Nicolescu, S., and Allen, C.M. (2003). Combined single-grain (U-Th)/He and U/Pb dating of detrital zircons from the Navajo Sandstone, Utah. *Geology*, v. 31, p. 761-764. https://doi.org/10.1130/G19653.1.

Reiners, P.W., Farley, K.A., Hickes, H.J. (2002). He diffusion and (U-Th)/He thermochronomtery of zircon: initial results from Fish Canyon Tuff and Gold Butte. *Tectonophysics*, 349, 297-308. https://doi.org/10/1016/S0040-1951(02)00058-6.

Reiners, P. W., & Brandon, M. T. (2006). Using thermochronology to understand orogenic erosion. *Annual Review of Earth and Planetary Sciences*, *34*(1), 419–466.

Reiners, P. W., Spell, T. L., Nicolescu, S., & Zanetti, K. A. (2004). Zircon (U-Th)/He thermochronometry: He diffusion and comparisons with 40Ar/39Ar dating. *Geochimica et Cosmochimica Acta*, *68*(8), 1857–1887. https://doi.org/10.1016/j.gca.2003.10.021

Ruhl, K. W., & Hodges, K. V. (2005). The use of detrital mineral cooling ages to evaluate steady state assumptions in active orogens: An example from the central Nepalese Himalaya. *Tectonics*, *24*(4), 2004TC001712. https://doi.org/10.1029/2004TC001712

Sakai, H., Sawada, M., Takigami, Y., Orihashi, Y., Danhara, T., Iwano, H., Kuwahara, Y., Dong, Q., Cai, H. and Li, J. (2005), Geology of the summit limestone of Mount Qomolangma (Everest) and cooling history of the Yellow Band under the Qomolangma detachment. Island Arc, 14: 297-310. https://doi.org/10.1111/j.1440-1738.2005.00499.x

Sakai, H., Iwano, H., Danhara, T., Takigami, Y., Rai, S. M., Upreti, B. N., & Hirata, T. (2013). Rift-related origin of the Paleoproterozoic Kuncha Formation, and cooling history of the Kuncha nappe and Taplejung granites, eastern Nepal Lesser Himalaya: a multichronological approach. *Island Arc*, *22*(3), 338-360.

Sanyal, P., Bhattacharya, S. K., Kumar, R., Ghosh, S. K., & Sangode, S. J. (2004). Mio–Pliocene monsoonal record from Himalayan foreland basin (Indian Siwalik) and its relation to vegetational change. *Palaeogeography, Palaeoclimatology, Palaeoecology*, *205*(1–2), 23–41. https://doi.org/10.1016/j.palaeo.2003.11.013

Saylor, J. E., & Sundell, K. E. (2016). Quantifying comparison of large detrital geochronology data sets. Geosphere, 12(1), 203-220.

Saylor, J. E., Jordan, J. C., Sundell, K. E., Wang, X., Wang, S., & Deng, T. (2017). Topographic growth of the Jishi Shan and its impact on basin and hydrology evolution, NE Tibetan Plateau. *Basin Research*, *30*(3), 544–563. https://doi.org/10.1111/bre.12264

Schultz, M. H., Hodges, K. V., Ehlers, T. A., Van Soest, M., & Wartho, J. A. (2017). Thermochronologic constraints on the slip history of the South Tibetan detachment system in the Everest region, southern Tibet. *Earth and Planetary Science Letters*, *459*, 105-117.

Schultz, M. H. (2017). *The Late Cenozoic Climatic and Tectonic Evolution of the Mount Everest Region, Central Himalaya*. [Doctoral Dissertation, Arizona State University].

Searle, M., & Cottle, J. (2024). Himalayan Leucogranites: Field Relationships and Tectonics. *Elements*, *20*(6), 373–380. https://doi.org/10.2138/gselements.20.6.373

Shangguan, D., Liu, S., Ding, Y., Wu, L., Deng, W., Guo, W., Wang, Y., Xu, J., Yao, X., Guo, Z., & Zhu, W. (2014). Glacier changes in the Koshi River basin, central Himalaya, from 1976 to 2009, derived from remote-sensing imagery. *Annals of Glaciology*, *55*(66), 61–68. https://doi.org/10.3189/2014AoG66A057

Sherpa, T. Z. L., DeCelles, P. G., Carrapa, B., Schoenbohm, L. M., & Wolpert, J. (2022). Bhumichula plateau: A remnant high-elevation low-relief surface in the Himalayan thrust belt of western Nepal. *GSA Bulletin*. https://doi.org/10.1130/B36481.1

Sherpa, T. Z. L., DeCelles, P. G., Gehrels, G. E., & Pokhrel, C. (2024). Tectonic Evolution of the Himalayan Fold-Thrust Belt in the Okhaldhunga Region, Eastern Nepal. *Tectonics*, *43*(12), e2024TC008457. https://doi.org/10.1029/2024TC008457

Sonam, & Jain, V. (2018). Geomorphic effectiveness of a long profile shape and the role of inherent geological controls in the Himalayan hinterland area of the Ganga River basin, India. *Geomorphology*, *304*, 15–29. https://doi.org/10.1016/j.geomorph.2017.12.022

Stock, G. M., Ehlers, T. A., & Farley, K. A. (2006). Where does sediment come from? Quantifying catchment erosion with detrital apatite (U-Th)/He thermochronometry. *Geology*, *34*(9), 725. https://doi.org/10.1130/G22592.1

Streule, M. J., Carter, A., Searle, M. P., & Cottle, J. M. (2012). Constraints on brittle field exhumation of the Everest-Makalu section of the Greater Himalayan Sequence: Implications for models of crustal flow. *Tectonics*, *31*(3). https://doi.org/10.1029/2011TC003062

Sundell, K. E., & Saylor, J. E. (2017). Unmixing detrital geochronology age distributions. *Geochemistry, Geophysics, Geosystems*, *18*(8), 2872–2886. https://doi.org/10.1002/2016GC006774

Van Der Beek, P., & Schildgen, T. F. (2022). *Short Communication: Age2exhume – A Matlab script to calculate steady-state vertical exhumation rates from thermochronologic ages in regional datasets and application to the Himalaya*. Geochronological data analysis/statistics/modelling. https://doi.org/10.5194/egusphere-2022-888

Vermeesch, P. (2013). Multi-sample comparison of detrital age distributions. *Chemical Geology*, *341*, 140–146. https://doi.org/10.1016/j.chemgeo.2013.01.010

Vezzoli, G., Garzanti, E., Limonta, M., Andò, S., & Yang, S. (2016). Erosion patterns in the Changjiang (Yangtze River) catchment revealed by bulk-sample versus single-mineral provenance budgets. *Geomorphology*, *261*, 177–192. https://doi.org/10.1016/j.geomorph.2016.02.031

Wang, A., Garver, J. I., Wang, G., Smith, J. A., & Zhang, K. (2010). Episodic exhumation of the Greater Himalayan Sequence since the Miocene constrained by fission track thermochronology in Nyalam, central Himalaya. *Tectonophysics*, *495*(3–4), 315–323. https://doi.org/10.1016/j.tecto.2010.09.037

Whipple, K., Adams, B., Forte, A., & Hodges, K. (2023). Eroding the Himalaya: Topographic and Climatic Control of Erosion Rates and Implications for Tectonics. *The Journal of Geology*, *131*(4), 265–288. https://doi.org/10.1086/731260

Whipple, K. (2009). The influence of climate on the tectonic evolution of mountain belts. *Nature Geoscience*, *2*(2), 97–104. https://doi.org/10.1038/ngeo413

Whipple, K., Shirzaei, M., Hodges, K. V., & Ramon Arrowsmith, J. (2016). Active shortening within the Himalayan orogenic wedge implied by the 2015 Gorkha earthquake. *Nature Geoscience*, *9*(9), 711–716. https://doi.org/10.1038/ngeo2797

Xu, W., Hughes, N. C., Liu, L., Zhang, W., & Liu, P. (2022). Paleogeographic Reconstruction of the Paleozoic Lhasa Terrane Through Detrital Zircon Mixing Modeling. *Geophysical Research Letters*, *49*(21), e2022GL100160. https://doi.org/10.1029/2022GL100160

Yamada, R., Tagami, T., Nishimura, S., & Ito, H. (1995). Annealing kinetics of fission tracks in zircon: An experimental study. *Chemical Geology*, *122*(1–4), 249–258. https://doi.org/10.1016/0009-2541(95)00006-8

Yin, A., & Harrison, T. M. (2000). Geologic Evolution of the Himalayan-Tibetan Orogen. *Annual Review of Earth and Planetary Sciences*, *28*(1), 211–280. https://doi.org/10.1146/annurev.earth.28.1.211

Figure 1.

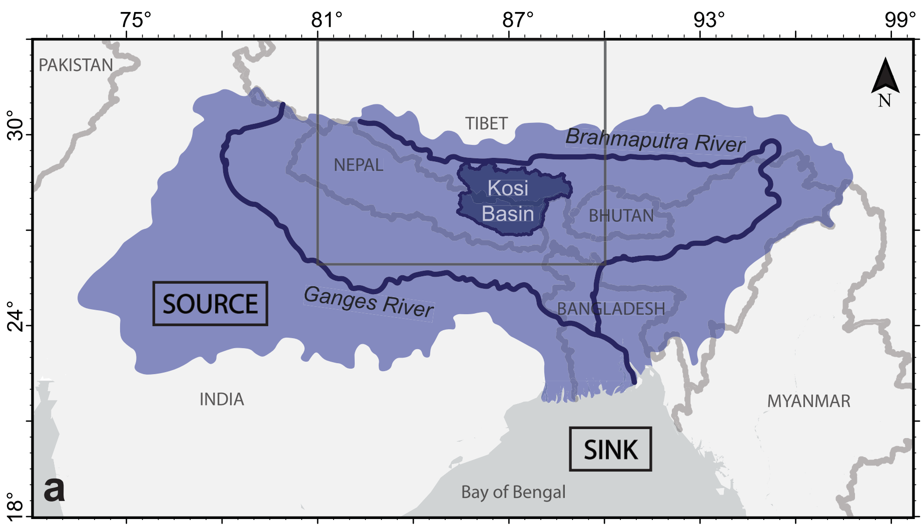

75°
81°
87°
93°
99°
30°
24°
18°
PAKISTAN
TIBET
NEPAL
Kosi Basin
BHUTAN
Brahmaputra River
Ganges River
BANGLADESH
SOURCE
INDIA
MYANMAR
SINK
Bay of Bengal
N
a

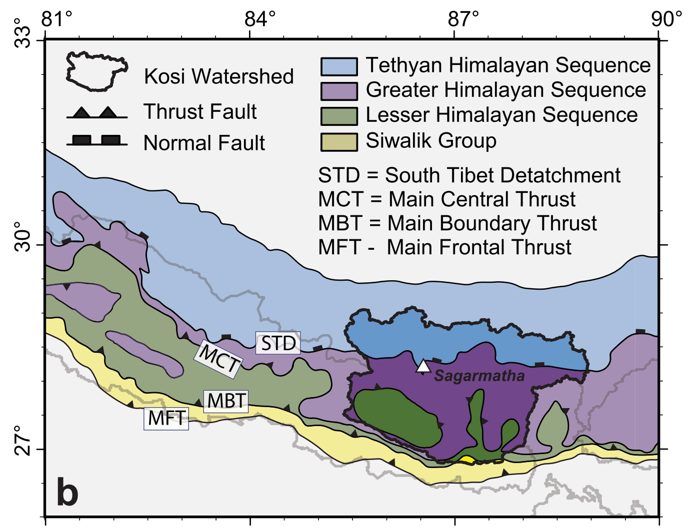

81°
84°
87°
90°
33°
30°
27°
Kosi Watershed
Thrust Fault
Normal Fault
Tethyan Himalayan Sequence
Greater Himalayan Sequence
Lesser Himalayan Sequence
Siwalik Group
STD = South Tibet Detatchment
MCT = Main Central Thrust
MBT = Main Boundary Thrust
MFT - Main Frontal Thrust
STD
MCT
MBT
MFT
Sagarmatha
b

Figure 2.

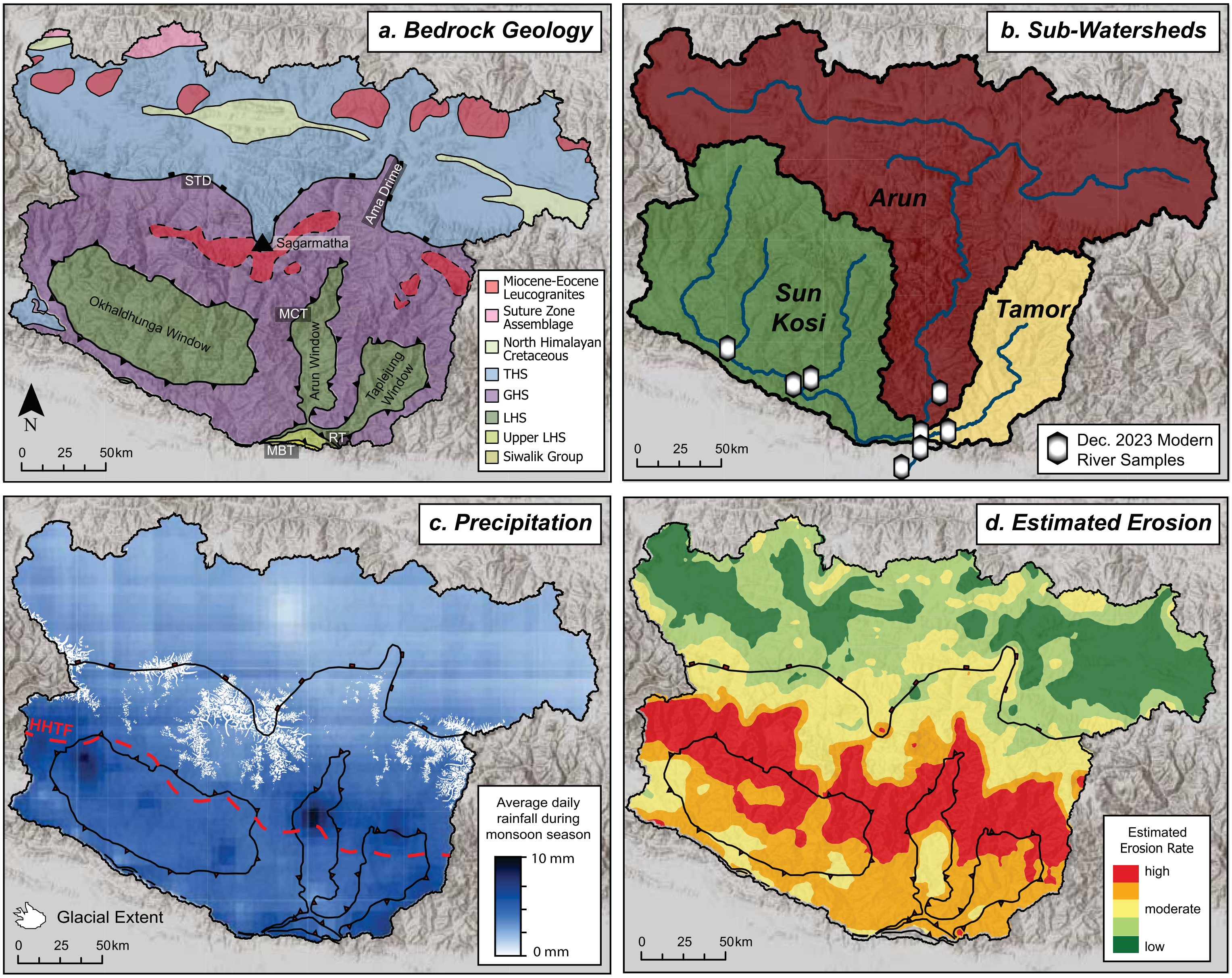
a. Bedrock Geology
STD
Ama Drime
Sagarmatha
MCT
Okhaldhunga Window
Arun Window
Taplejung Window
RT
MBT
N
0 25 50km
Miocene-Eocene Leucogranites
Suture Zone Assemblage
North Himalayan Cretaceous
THS
GHS
LHS
Upper LHS
Siwalik Group
b. Sub-Watersheds
Arun
Sun Kosi
Tamor
0 25 50km
Dec. 2023 Modern River Samples
c. Precipitation
HHTF
Average daily rainfall during monsoon season
10 mm
0 mm
Glacial Extent
0 25 50km
d. Estimated Erosion
Estimated Erosion Rate
high
moderate
low
0 25 50km

Figure 3.

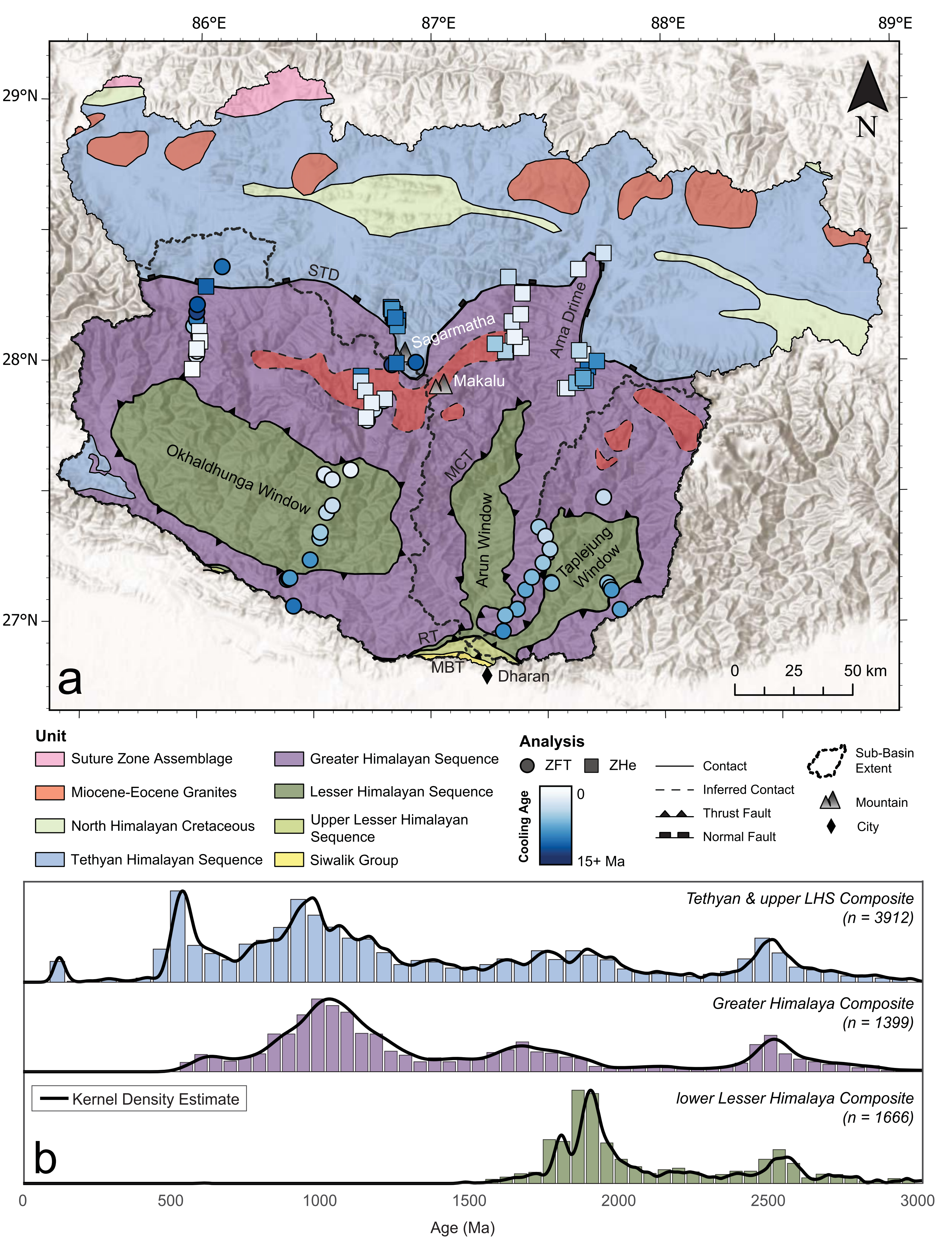
86°E
87°E
88°E
89°E
29°N
28°N
27°N
N
STD
Sagarmatha
Makalu
Ama Drime
Okhaldhunga Window
MCT
Arun Window
Taplejung Window
RT
MBT
Dharan
0 25 50 km
a
Unit
Suture Zone Assemblage
Miocene-Eocene Granites
North Himalayan Cretaceous
Tethyan Himalayan Sequence
Greater Himalayan Sequence
Lesser Himalayan Sequence
Upper Lesser Himalayan Sequence
Siwalik Group
Analysis
ZFT
ZHe
Cooling Age
0
15+ Ma
Contact
Inferred Contact
Thrust Fault
Normal Fault
Sub-Basin Extent
Mountain
City
Tethyan & upper LHS Composite
(n = 3912)
Greater Himalaya Composite
(n = 1399)
Kernel Density Estimate
lower Lesser Himalaya Composite
(n = 1666)
b
0
500
1000
1500
2000
2500
3000
Age (Ma)

Figure 4.

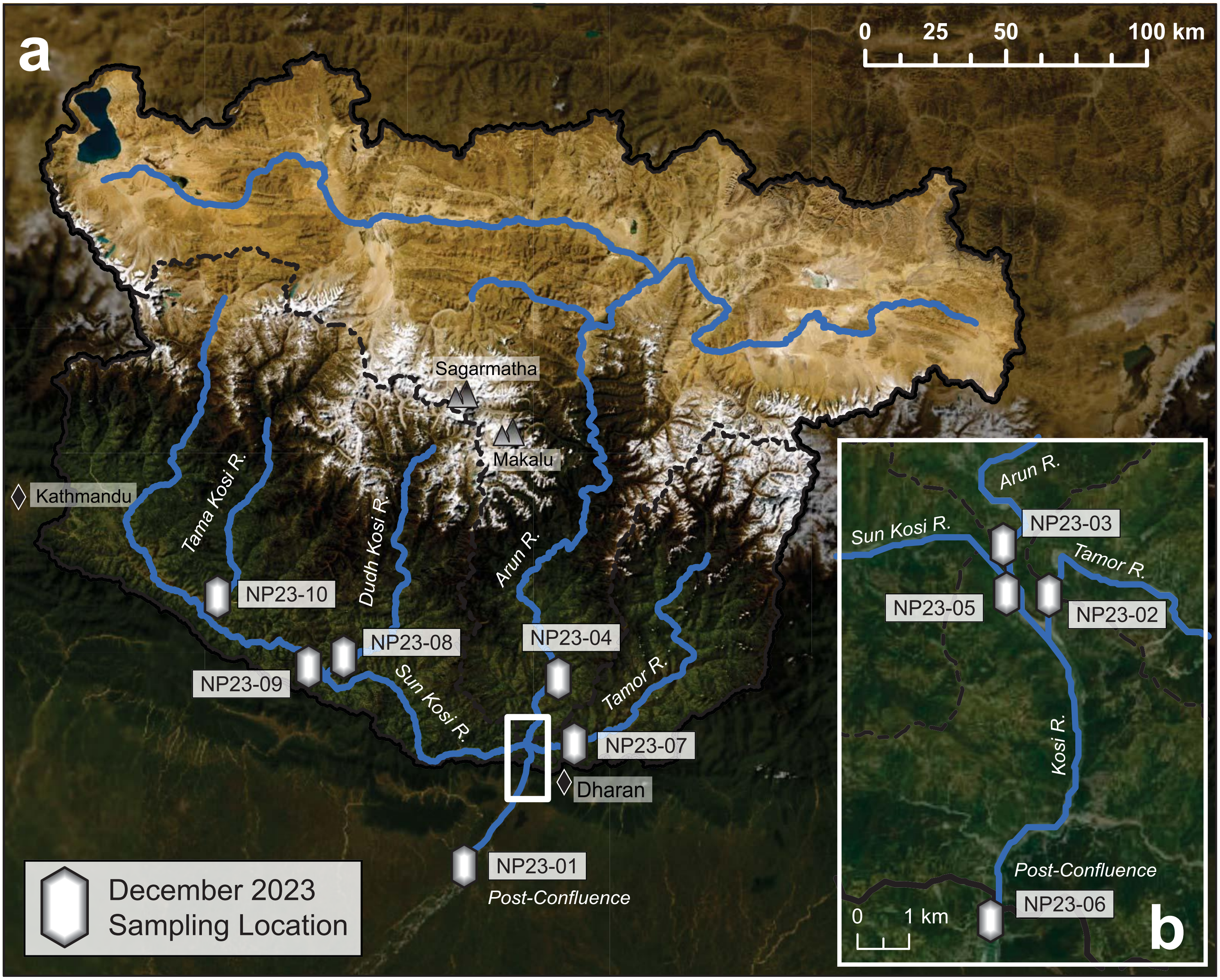
a
0 25 50 100 km
Sagarmatha
Makalu
Kathmandu
Tama Kosi R.
Dudh Kosi R.
Arun R.
NP23-10
NP23-08
NP23-09
NP23-04
Sun Kosi R.
Tamor R.
NP23-07
Dharan
NP23-01
Post-Confluence
December 2023
Sampling Location
Arun R.
Sun Kosi R.
NP23-03
Tamor R.
NP23-05
NP23-02
Kosi R.
Post-Confluence
NP23-06
0 1 km
b

Figure 5.

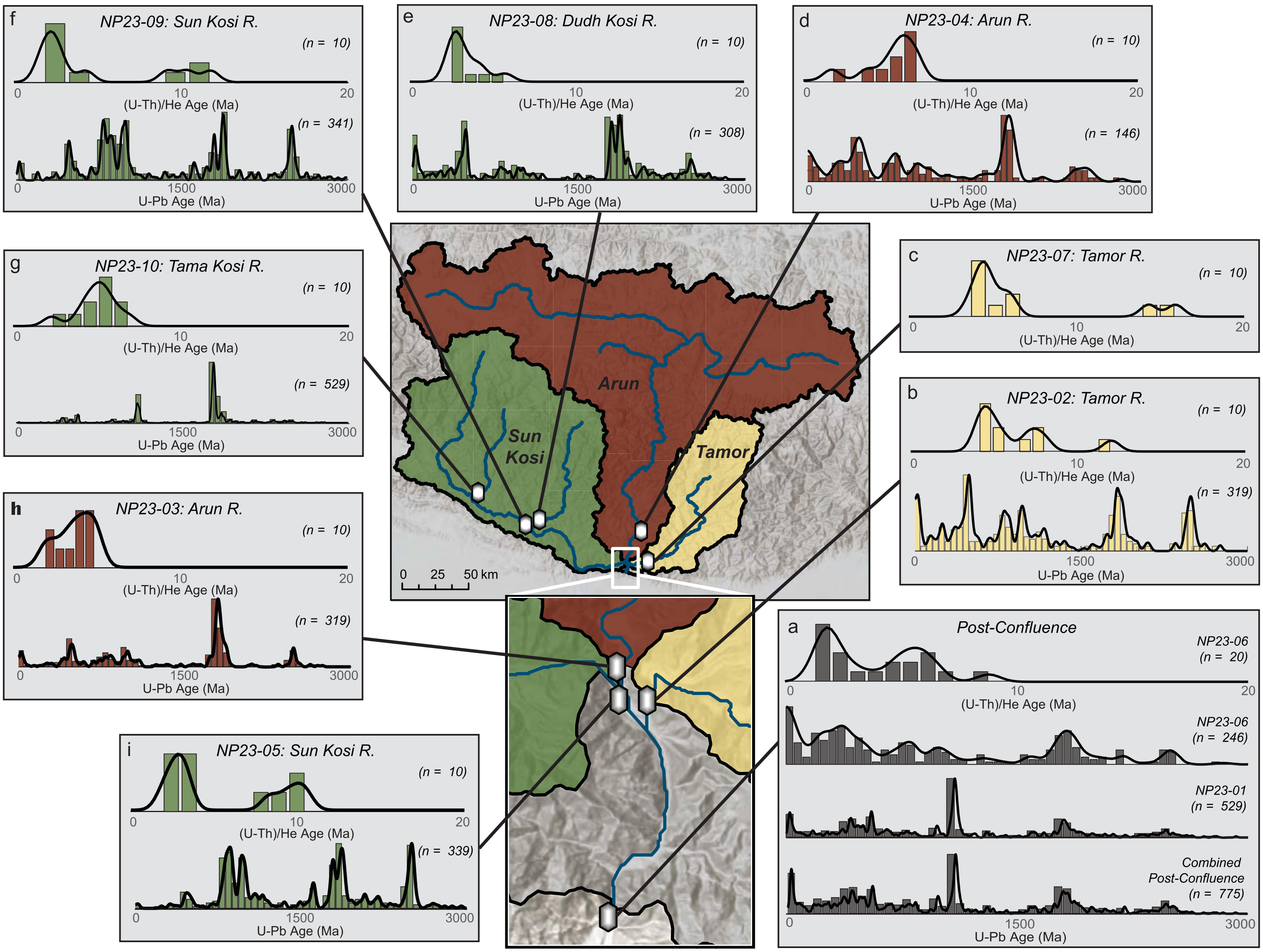

f
NP23-09: Sun Kosi R.
(n = 10)
(U-Th)/He Age (Ma)
(n = 341)
U-Pb Age (Ma)
e
NP23-08: Dudh Kosi R.
(n = 10)
(U-Th)/He Age (Ma)
(n = 308)
U-Pb Age (Ma)
d
NP23-04: Arun R.
(n = 10)
(U-Th)/He Age (Ma)
(n = 146)
U-Pb Age (Ma)
g
NP23-10: Tama Kosi R.
(n = 10)
(U-Th)/He Age (Ma)
(n = 529)
U-Pb Age (Ma)
c
NP23-07: Tamor R.
(n = 10)
(U-Th)/He Age (Ma)
b
NP23-02: Tamor R.
(n = 10)
(U-Th)/He Age (Ma)
(n = 319)
U-Pb Age (Ma)
Arun
Sun Kosi
Tamor
0 25 50 km
h
NP23-03: Arun R.
(n = 10)
(U-Th)/He Age (Ma)
(n = 319)
U-Pb Age (Ma)
i
NP23-05: Sun Kosi R.
(n = 10)
(U-Th)/He Age (Ma)
(n = 339)
U-Pb Age (Ma)
a
Post-Confluence
NP23-06
(n = 20)
(U-Th)/He Age (Ma)
NP23-06
(n = 246)
NP23-01
(n = 529)
Combined Post-Confluence
(n = 775)
U-Pb Age (Ma)

Figure 6.

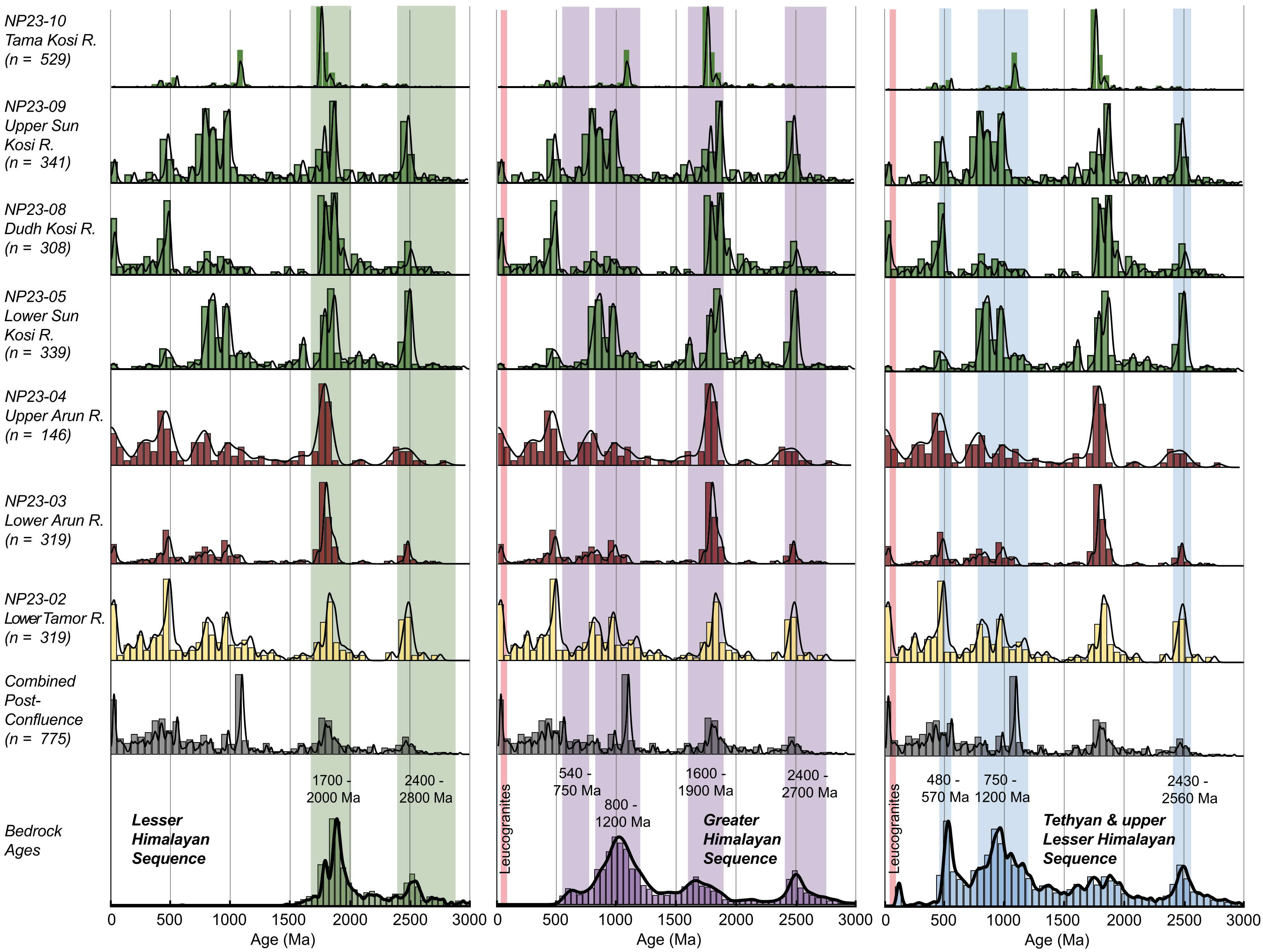
NP23-10
Tama Kosi R.
(n = 529)
NP23-09
Upper Sun
Kosi R.
(n = 341)
NP23-08
Dudh Kosi R.
(n = 308)
NP23-05
Lower Sun
Kosi R.
(n = 339)
NP23-04
Upper Arun R.
(n = 146)
NP23-03
Lower Arun R.
(n = 319)
NP23-02
Lower Tamor R.
(n = 319)
Combined
Post-
Confluence
(n = 775)
Bedrock
Ages
1700 -
2000 Ma
2400 -
2800 Ma
Lesser
Himalayan
Sequence
Leucogranites
540 -
750 Ma
800 -
1200 Ma
1600 -
1900 Ma
2400 -
2700 Ma
Greater
Himalayan
Sequence
Leucogranites
480 -
570 Ma
750 -
1200 Ma
2430 -
2560 Ma
Tethyan & upper
Lesser Himalayan
Sequence
0
500
1000
1500
2000
2500
3000
Age (Ma)

Figure 7.

Zircon (U-Th)/He Ages from Modern Rivers

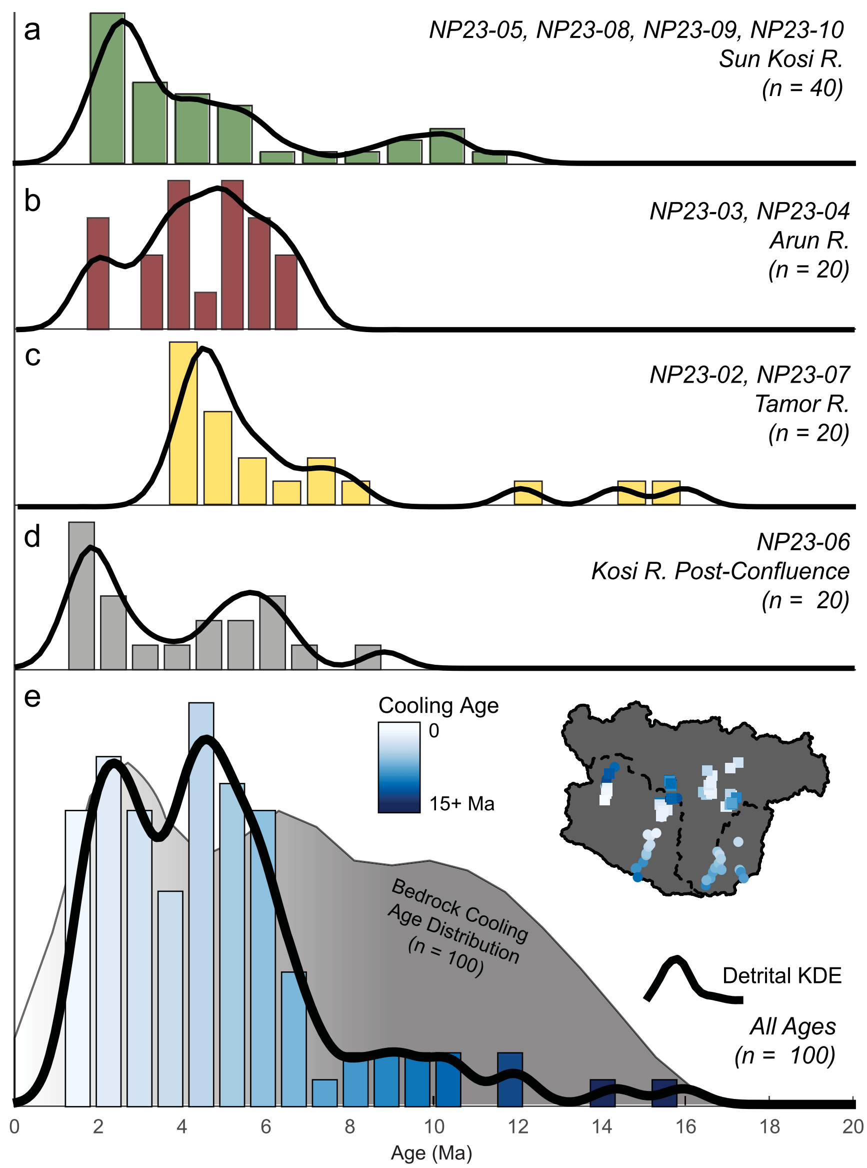

Figure 8.

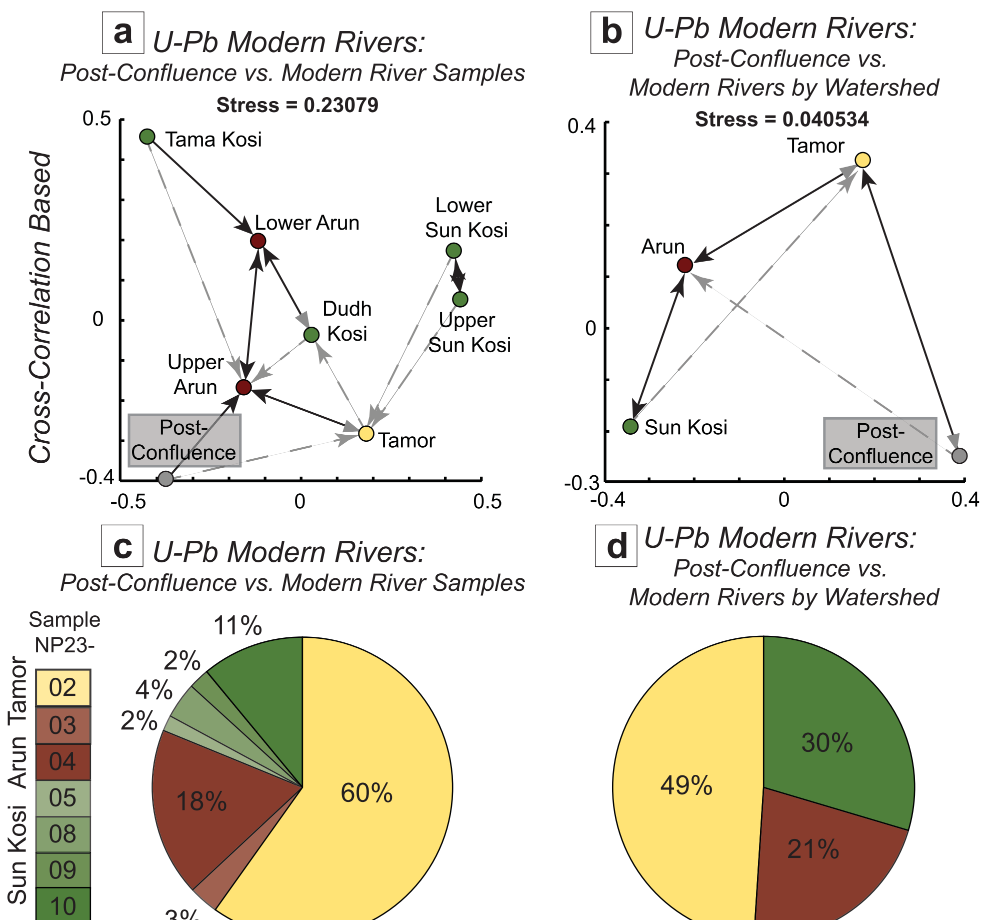
a
U-Pb Modern Rivers:
Post-Confluence vs. Modern River Samples
Stress = 0.23079
Cross-Correlation Based
0.5
0
-0.4
-0.5
0
0.5
Tama Kosi
Lower Arun
Lower
Sun Kosi
Dudh
Kosi
Upper
Sun Kosi
Upper
Arun
Tamor
Post-
Confluence
b
U-Pb Modern Rivers:
Post-Confluence vs.
Modern Rivers by Watershed
Stress = 0.040534
0.4
0
-0.3
-0.4
0
0.4
Tamor
Arun
Sun Kosi
Post-
Confluence
c
U-Pb Modern Rivers:
Post-Confluence vs. Modern River Samples
Sample
NP23-
Tamor
Arun
Sun Kosi
02
03
04
05
08
09
10
11%
2%
4%
2%
18%
60%
3%
d
U-Pb Modern Rivers:
Post-Confluence vs.
Modern Rivers by Watershed
30%
49%
21%

Figure 9.

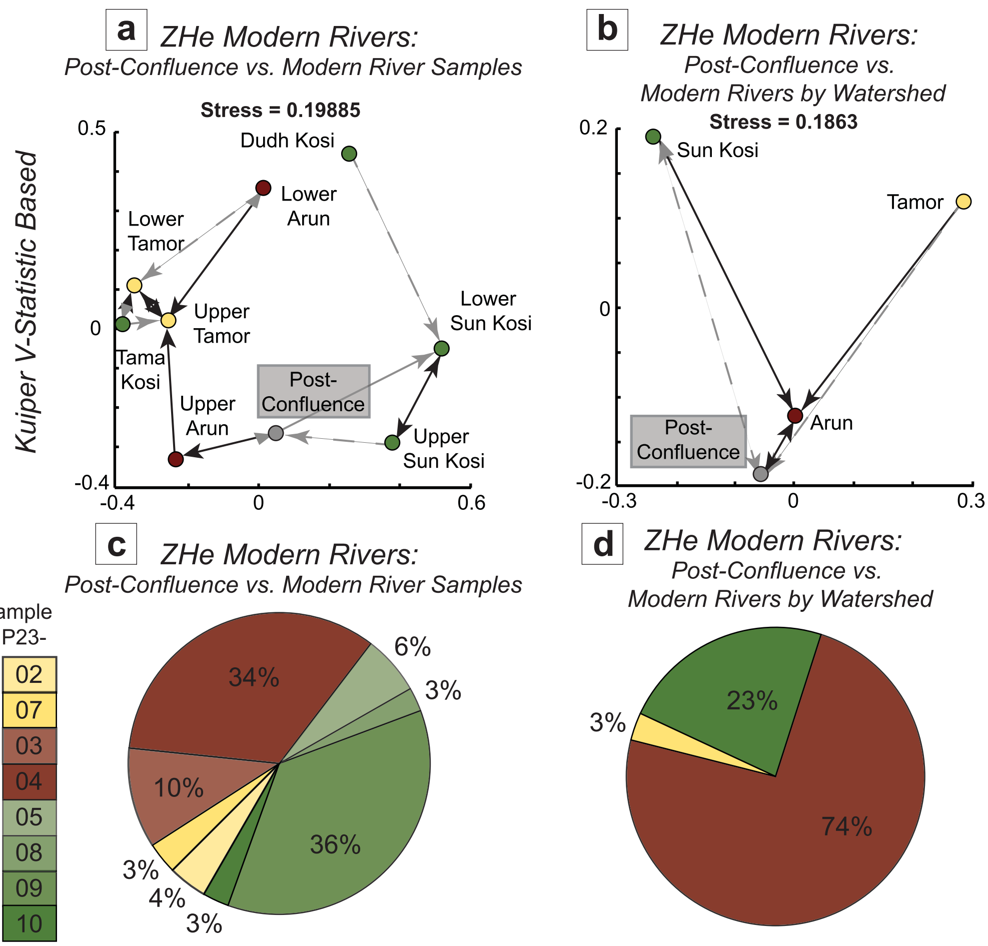
a
ZHe Modern Rivers:
Post-Confluence vs. Modern River Samples
Stress = 0.19885
Kuiper V-Statistic Based
0.5
0
-0.4
-0.4
0
0.6
Dudh Kosi
Lower Arun
Lower Tamor
Upper Tamor
Tama Kosi
Lower Sun Kosi
Post-Confluence
Upper Arun
Upper Sun Kosi
b
ZHe Modern Rivers:
Post-Confluence vs.
Modern Rivers by Watershed
Stress = 0.1863
0.2
0
-0.2
-0.3
0
0.3
Sun Kosi
Tamor
Arun
Post-Confluence
c
ZHe Modern Rivers:
Post-Confluence vs. Modern River Samples
Sample NP23-
Tamor
Arun
Sun Kosi
02
07
03
04
05
08
09
10
34%
6%
3%
10%
36%
3%
4%
3%
d
ZHe Modern Rivers:
Post-Confluence vs.
Modern Rivers by Watershed
23%
3%
74%

Figure 10.

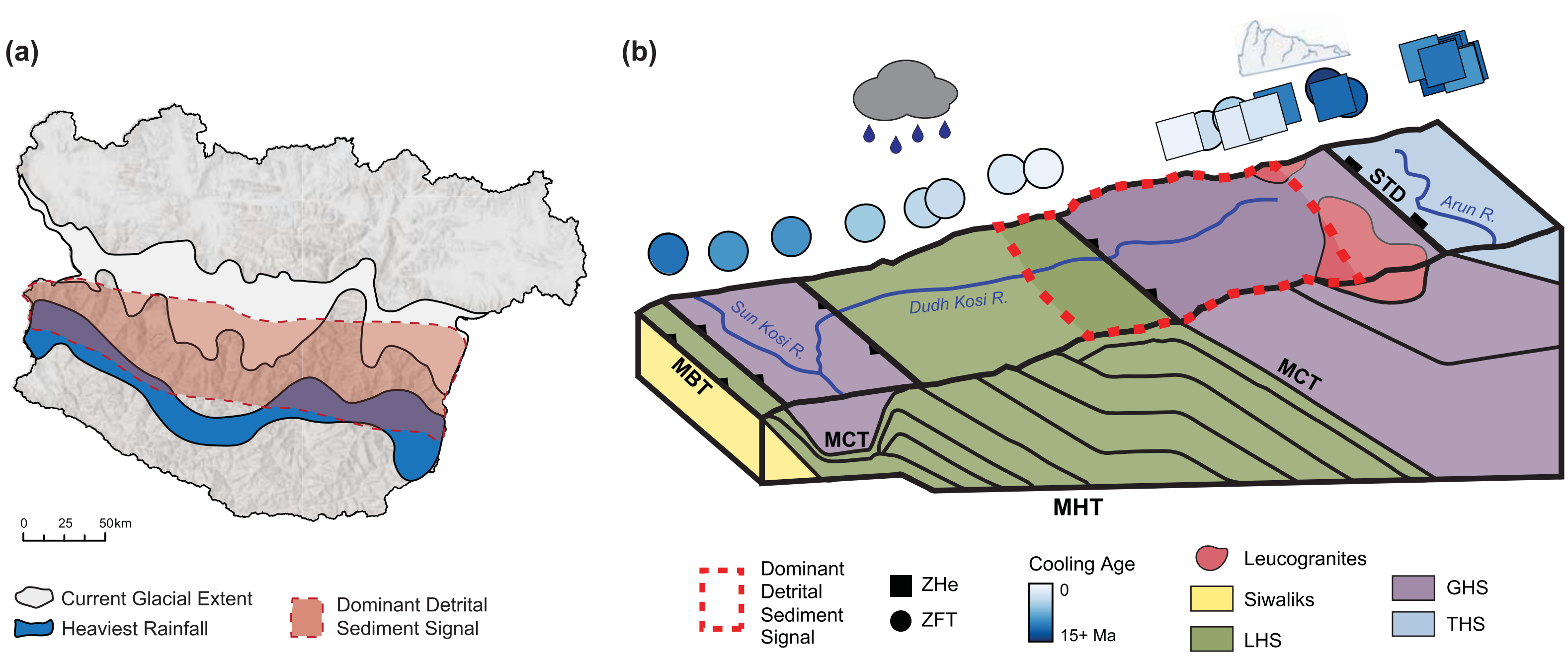

(a)
0 25 50km
Current Glacial Extent
Heaviest Rainfall
Dominant Detrital Sediment Signal
(b)
Sun Kosi R.
Dudh Kosi R.
Arun R.
STD
MBT
MCT
MCT
MHT
Dominant Detrital Sediment Signal
ZHe
ZFT
Cooling Age
0
15+ Ma
Leucogranites
Siwaliks
LHS
GHS
THS